



# Microstructural, Mechanical and Wear Behavior of HVOF and Cold-Sprayed High-Entropy Alloys (HEAs) Coatings

A. Silvello<sup>1</sup> · P. Cavaliere<sup>2</sup> · S. Yin<sup>3</sup> · R. Lupoi<sup>3</sup> · I. Garcia Cano<sup>1</sup> · S. Dosta<sup>4</sup>

Submitted: 22 June 2021 / in revised form: 22 October 2021 / Accepted: 8 November 2021 / Published online: 21 January 2022  
© ASM International 2021

**Abstract** HEAs powders, unlike standard alloys which contain one or two base elements, are new alloys that contain multiple elements in the same quantity. These materials have outstanding physical and mechanical properties and for this reason, are of great interest in the material science community for their application in advanced industrial sectors. In this investigation, cold spray (CS) and high-velocity oxy fuel (HVOF) processes were used to deposit Cantor alloy (FeCoCrNiMn) coatings. Starting feedstock powders were thoroughly characterized in terms of size, shape, phase and elastic modulus. For CS process, the coating deposition efficiency and porosity could be optimized by varying gas pressure, gas

temperature and stand-off distance. In the case of HVOF process, stand-off distance influenced the thickness of the coatings. Besides, on the optimized CS and HVOF coatings, corrosion tests in 3.5% NaCl solution, as well as rubber wheel, ball on disk and jet erosion tests were carried out to evaluate their wear behavior. Also, to benchmark the corrosion and wear behavior of optimized coatings, the results were compared to 316L and C-Steel bulks. The tribological study shows that Cantor alloy coatings deposited via CS and HVOF are promising to protect parts and components in a harsh environment.

**Keywords** cold spray · corrosion protection · erosion resistant coatings · HVOF · HEAs · tribology · wear

This article is part of a special topical focus in the Journal of Thermal Spray Technology on High Entropy Alloy and Bulk Metallic Glass Coatings. The issue was organized by Dr. Andrew S.M. Ang, Swinburne University of Technology; Prof. B.S. Murty, Indian Institute of Technology Hyderabad; Distinguished Prof. Jien-Wei Yeh, National Tsing Hua University; Prof. Paul Munroe, University of New South Wales; Distinguished Prof. Christopher C. Berndt, Swinburne University of Technology. The issue organizers were mentored by Emeritus Prof. S. Ranganathan, Indian Institute of Sciences.

✉ A. Silvello  
asilvello@cptub.eu

- <sup>1</sup> Thermal Spray Center (CPT), University of Barcelona, Martí i Franqués 1, 08028 Barcelona, Spain
- <sup>2</sup> Department of Innovation Engineering, University of Salento, via per Arnesano, 73100 Lecce, Italy
- <sup>3</sup> Department of Mechanical, Manufacturing & Biomedical Engineering, Trinity College Dublin, The University of Dublin, Parsons Building, Dublin, Ireland
- <sup>4</sup> Materials Science Department, University of Barcelona, Martí i Franqués 1, 08028 Barcelona, Spain

## Introduction

HEAs powders are a new class of materials that contain multiple principal elements in the same quantity, unlike traditional alloys, which contain one or two base elements. Combining the effect of high entropy, lattice torsion and cocktail effect, HEAs have been reported to have excellent physical, chemical and mechanical properties such as high hardness, thermal stability, ductility, high wear and corrosion resistance (Ref 1, 2). Yeh et al. (Ref 3) and Cantor et al. (Ref 4) have defined HEAs and established the convention of at least five principal elements, thus the total number of possible HEAs composition is significantly high (Ref 5). It is undeniable that HEAs have received the attention of scientific community thanks to their potential industrial applications. As a consequence of their special phase structure, they have excellent mechanical properties, as well as remarkable corrosion resistance performances. Compared to conventional alloys, HEAs have been shown

many advantages. Zhang et al. (Ref 6) have reviewed and discussed HEAs properties in terms of physical, magnetic, chemical and mechanical behavior, concluding that the corrosion resistance of Cu<sub>0.5</sub>NiAlCoCrFeSi alloy is better than that of the conventional 304-stainless steel. In their corrosion analysis, Qiu et al (Ref 7) preferred to term these new alloys as CCAs (compositionally complex alloys), because some HEAs did not have high configurational entropies and present the formation of secondary phases. Even if these authors have chosen to use a different definition, the conclusion of their study is the same; the corrosion resistance of HEAs is in the same range of austenitic/ferritic stainless steel.

On these premises, it is no doubt true that investigating on advanced industrial applications of HEAs, such as boilers and tubes in power or waste plants, could open up new scenarios. According to Kumar et al. (Ref 8), the failure of a boiler is big hazard to the effectiveness of the boiler in the power plants. In their work, it is shown how overall economic loss due to all the types of corrosion accounts to US\$ 6500 million annually. This aspect limits the availability of a plant and hence rises its maintenance and investment costs.

Coatings deposited via traditional thermal spray process, such as HVOF, have always been used in harsh environment to improve corrosion and wear resistance of a substrate material (Ref 9–13). To protect metallic boiler parts, usually produced from carbon steel, Ni-based superalloys, nickel aluminide and NiCrAlY coatings have been successfully deposited (Ref 14–16). In (Ref 17), Singh et al. have reviewed corrosion performance of different coatings produced via different techniques, while a complete analysis about corrosion resistance of thermal spray coatings was carried out from Sadeghi et al. (Ref 18). In particular, they have addressed the issue not only from a technical point of view, but also studying challenges, opportunities and future developments of coatings for corrosion and wear resistance. In general terms, Katranidis et al. (Ref 19, 20) have investigated the influence of HVOF process parameters on porosity, residual stresses, thickness and so on. They have concluded that using a new-generation HVOF torch, the decarburization and oxidation effects on mechanical properties of the coatings are minimal.

Thus, it is clear that surface coatings can improve mechanical properties of the coated part. For this reason, the next advance for scientific and industrial communities is to investigate new promising starting feedstock powders deposited via thermal spray processes, such as HEAs. Li et al. (Ref 21) have studied coatings based on HEAs alloys, discussing design principles, process fabrication, post heat treatments and potential applications. Also, these authors have divided HEAs coatings into three categories (metallic, ceramic and composite coatings), and then they have listed

both the most common and emergent processes to fabricate them.

Among these emergent processes, cold spray (CS) is different from traditional thermal spray processes because, to deposit coatings, it uses kinetic energy rather than thermal energy. CS is used to fabricate coatings or to repair damaged parts (Ref 22–24), and it is well-known as a thick metal layer deposition technique. It works at relatively low processing temperatures, maintaining the initial phase of powders and thus, can be avoided the defects of conventional thermal spray processes (Ref 25–28). Moreover, CS has been used for advanced industrial purpose such as to improve mechanical and microstructural properties of coatings to rise up efficiency, reliability and productivity of boilers and tubes of power/nuclear plants. In particular, the chambers of Tokamak (Ref 29) are coated with dense coatings of W or W-Cr-based alloys. The advantages of using CS process for this task have been no oxidation, low porosity and high adhesion strength.

Recently, CS process has been used to deposit HEA Cantor (FeCrMnNiCo) alloy (Ref 30, 31). These two studies have confirmed that CS can be used to produce a thick HEA coating with low porosity that are harder than the as-received starting powders, without any phase transformation and finally, with a lower wear rate than laser cladded one. Additionally, the investigation of the high-temperature oxidation behavior of this HEA coating at 700 °C and 900 °C has shown that it presents more favorable internal oxidation than the similar compositions HEAs bulk. Lehtonen et al. (Ref 32) sprayed via CS a four components alloy (FeCrMnNi, without Co) to study if it is possible to replace stainless steels coating in nuclear industries. They have deposited a HEAs alloys without Co because of nuclear applications, due to the possible activation to <sup>60</sup>Co in the presence of neutrons, it is better to avoid it. However, even without Co, the FeCrMnNi cold-sprayed coating has shown high hardness, low porosity and in general terms, excellent mechanical properties.

In this fast-moving scenario, the aims of this work are to study microstructural, and mechanical properties, as well as corrosion and wear resistance, of different coatings produced via HVOF and CS processes and to evaluate their potential application for advanced industrial purposes. To reach these objectives, Cantor starting powder was characterized in terms of size, phases, shape and so on, while each produced coating was characterized carrying out different wear tests. The results obtained need further investigation but are encouraging and confirm that the use of thermally sprayed HEAs powders is viable for innovative industrial applications.

The aim of the present paper is to understand how processing parameters of two different deposition techniques, HVOF and CS, can be optimized in order to obtain

sound bulk HEA coatings. In addition, how to improve the coatings' mechanical properties by varying process parameters for these two different deposition techniques is a focus issue of the present study. After focusing on different porosity levels, the obtained results in terms of wear and corrosion resistance are underlined as fundamental properties for the deposition processes optimization.

## Materials and Methods

HEAs powders characterization, as well as coatings deposition, characterization and testing (adhesion strength, hardness, corrosion resistance, rubber wheel, ball on disk, jet erosion test), were carried out at the facilities of the Thermal Spray Center (CPT) at the University of Barcelona (Barcelona, ES). All the tests were performed on the cold-sprayed and HVOF samples. Also, the results were compared to 316L and low C steel bulks (CM4 Ingeniería S.L., Barcelona, ES, chemical composition in Table 1) in order to obtain benchmark values for the coatings; 316L and low C steel bulks have the same dimensions of the coated substrate (50 × 20 × 5 mm).

### Powders Characterization

HEAs powders (FeCrCoMnNi known as “Cantor alloy” were provided by Vilory Advanced Materials Technology Ltd, CN). Powders were characterized by particle size distribution, shape, chemical composition, XRD phase analysis, apparent density and flow rate.

Laser scattering (LS) technique was used for particle size distribution determination in a Beckman Coulter LS 13 320 (Brea, CA, USA) equipment, in accordance with the ASTM B822-02 on dry via mode. Inductively couple plasma (ICP) technique was used for chemical composition in an equipment PerkinElmer Optima ICP-OES 3200 RL (Waltham, MA, USA). The scanning electron microscopy (SEM, Thermo Fisher Phenom Pro Desktop, Eindhoven, NL) was used for image obtention. The technique x-ray diffractometry (XRD) in an equipment Malvern PANalytical X'Pert PRO MPD  $\theta/\theta$  Bragg–Brentano with X'Pert software (Malvern, United Kingdom) was used for phase analysis, with font of Cu  $K\alpha$  ( $\lambda=1.5418 \text{ \AA}$ ) and work power 45 kV–40 mA. The apparent density of the powders was measured in accordance with the ASTM B-212-99. The used powders sample had a volume of 40 cm<sup>3</sup>

approximately and has been followed the procedure listed in ASTM standard. The flow rate was measured in accordance with the ASTM B-213-03, applying the “Materials and Methods” This method consists in to weight out a 50g mass sample, pour the powders sample into the center of the funnel and start a stopwatch when the powders exit the orifice of the flowmeter funnel. When the last of the powders exit the funnel discharge orifice, the stopwatch is stopped. Both ASTM B-212-99 and ASTM B-213-03 tests were repeated 5 times. The equipment Mettler AE100 (Columbus, OH, USA) was used to weight the powders to calculate deposition efficiency. Also, nanohardness measurements of the starting particles were performed at 2.5 gf load on MTS Nano Indenter XP machine; the average value was taken from 25 indentations per sample (Table 2).

### Coatings Deposition

For cold spray depositions, PCS-100 equipment (Plasma Giken Co., Ltd., Osato, Saitama, JP) was used. HVOF coatings were produced using Oerlikon (Sulzer) Metco (Pfäffikon, CH) Diamond Jet Hybrid DJH 2600 equipment, with H as fuel gas. Before the deposition process, substrates were grit-blasted with alumina (F24), up to roughness  $Ra \approx 7 \mu\text{m}$ . The optimized process parameters used for cold spray and the HVOF process parameters are presented in Tables 3 and 4. The strategy deposition (the robot path on the substrate) is shown schematically in Fig. 1.

Tables 3 and 4 only list the optimized parameters used to produce CS and HVOF coatings. The optimization process of cold spray deposition parameters is shown in Table 8, while in the case of HVOF process, the different process parameters used are listed in Table 9.

In the case of cold spray deposition, the deposition efficiency (DE%) was measured taking into account the starting mass of powders into feeder, the remaining mass of powders in the feeder after the deposition, the mass of coated sample after the deposition, the starting substrate

**Table 2** Chemical composition (weight %) of FeCrCoMnNi (Cantor) alloy

	Fe	Cr	Co	Mn	Ni
FeCrCoMnNi	20.09	18.86	20.96	19.27	21.01

**Table 1** Chemical composition (wt.%) of 316L and C low C steel bulks

Bulk	C	Mn	Si	P	S	Cr	Ni	Mo	Fe
316L	< 0.035	< 2.0	< 0.075	< 0.040	< 0.030	17.00	12.00	2.50	Bal.
Low C steel	< 0.17	< 1.4	< 0.40	< 0.035	< 0.035	...	...	...	Bal.

**Table 3** Optimized parameters used for CGS process

Coating	Gas	Pressure	Temperature	Standoff distance	Robot speed	Powder feed	Step	Number of layers
CGS_N <sub>2</sub>	N <sub>2</sub>	7 MPa	1100 °C	15 mm	500 mm/s	2 rpm	1 mm	2

**Table 4** Parameters used for HVOF process

Coating	H <sub>2</sub> Flow rate	O <sub>2</sub> Flow rate	Air Flow rate	Powder feed	Standoff distance	Robot speed	Step	Number of layers
HVOF_250	10.6 l/s	3.6 l/s	5.7 l/s	0.50 g/s	250 mm	500 mm/s	5 mm	10

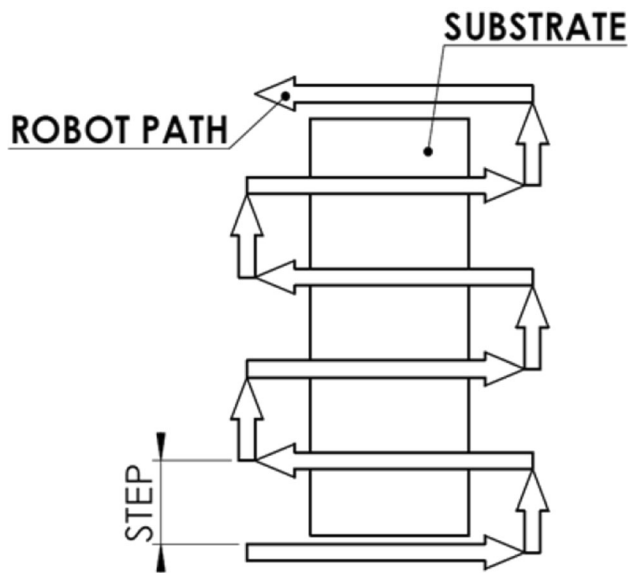


**Fig. 1** Deposition strategy, robot path

mass, the deposition time and the path and the time of robot over the substrate.

**Coatings Characterization**

Metallographic preparation was carried out in accordance with the ASTM E1920-03. The coatings microstructure was observed by employing the optical microscopy Leica DMI 5000M (OM). The Leica microscope image analyzer was used to calculate the coatings thickness. The porosity was calculated by grayscale threshold in OM images of the microstructure, according to the test method B of ASTM E2109-14, employing the ImageJ software. For each coating, seven porosity measurements were performed. The Shimadzu HMV (Tokyo, JP) was used for ten measures of microhardness in Vickers scale for each coating, with load 0.1 kgf (HV0.1). Also, etching of the optimized coatings was carried out adding some H<sub>2</sub>O droplets to NH<sub>3</sub> + HF +

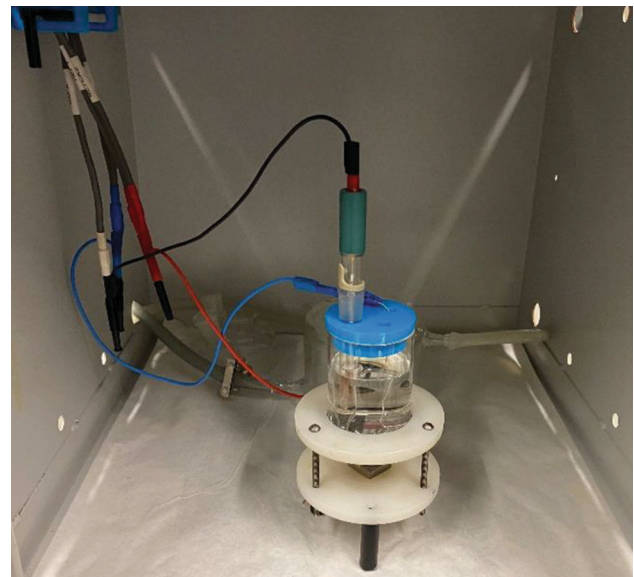


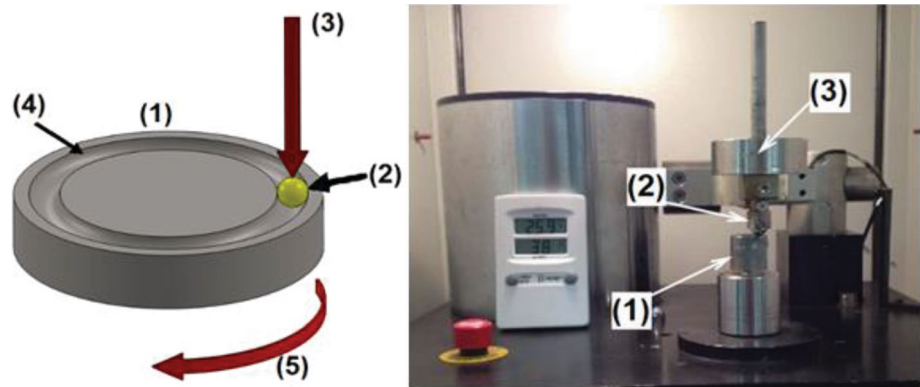
**Fig. 2** Real set-up for corrosion testing

H<sub>2</sub>SO<sub>4</sub> acid solution (1:1:1) and immersing the polished cross section of the sample.

**Corrosion Test**

Potentiodynamic polarization measurements were carried out, in accordance with the ASTM G59-97 and ASTM G102-89. To determine corrosion current density, polarization resistance, and corrosion rate of the coatings, a 3.5 wt.% NaCl water solution at room temperature was used. Two different samples of each coating and reference bulk were used for corrosion tests as working electrode, with exposed area of 1.0 cm<sup>2</sup>. The exposed surfaces were ground up to 1200 mesh and maximum roughness of Ra 0.3 μm. A saturated calomel (3.0 M KCl) was the reference electrode and a platinum was the counter electrode in the tests. A scan rate of 0.05 mV.s<sup>-1</sup> and a potential range from E<sub>corr</sub> ±25 mV were used to acquire the polarization resistance (R<sub>p</sub>), and E<sub>corr</sub> from – 250 to 1050 mV was

**Fig. 3** (a) Scheme and (b) Equipment for ball on disk testing, (1) Sample, (2) Ball, (3) Load, (4) Wear path on sample and (5) Rotation of sample



used to acquire the anodic (ba) and cathodic (bc) Tafel slopes. Figure 2 shows the experiment set-up.

### Adhesion Test

The adherence of the coatings was measured according to the ASTM C633-13. The adhesive agent used was the HTK Ultra Bond 100 (Hamburg, D), with measured adherence  $73.7 \pm 1.2$  MPa (four measures were done). The Servosis MCH-102 ME (Madrid, ES) equipment was used for the tests, and the results of the adherence were classified interpreting as adhesive, if the failure is completely between the coating and the substrate, cohesive, if the failure is intern of the coating and bonding failure, if the coating is completely not detached from the substrate.

### Sliding Wear Test (Ball on disk)

Ball on disk testing consists in the friction between a disk and a ball, without abrasive condition. The test was carried out in accordance with the ASTM G99-04, using a CM4 Enginierya S.L. (Barcelona, Es) equipment, as shown in Fig. 3. The surface of samples tested was previously prepared by grinding and polishing until the maximum roughness  $R_a$   $0.8 \mu\text{m}$ . The tests were performed at room temperature ( $27 \pm 2^\circ\text{C}$ ) and maximum 20% moisture without any lubricant. Process parameters are shown in Table 5. The coefficient of friction (CoF) between the WC-Co ball and the HEAs coating was measured, and this value was plotted (Table 6).

### Abrasive Wear Test (Rubber wheel)

In accordance with the ASTM G65-00, the low-stress abrasion test (rubber wheel) consists in an erosion wear with third body, where a rubber wheel rotates against the surface of the sample. This contact is done with determined

load and a constant feed of abrasive material between the wheel and the sample. Figure 4 shows how this abrasive test works and the equipment (CM4 Enginierya S.L., Barcelona, ES).  $\text{SiO}_2$  abrasive particles produced by Sibelco (Barcelona, ES) were fed in dry condition (less than 0.5% moisture). The mass of the sample was measured in different elapsed times of testing, using an equipment Mettler AE100 (Columbus, OH, USA).

The parameters of rubber wheel test are presented in Table X. The  $\text{SiO}_2$  has a granulometry of  $200 \mu\text{m}$ .

The results of the rubber wheel test are expressed using Eq. 1,

$$V = \text{Vol} / (F \cdot \omega \cdot 2 \cdot \pi \cdot R \cdot t) \quad (\text{Eq 1})$$

where  $V$  is the ratio of volume loss in  $\text{mm}^3\text{N}^{-1}\text{m}^{-1}$ ,  $\text{Vol}$  is the volume loss ( $\text{mm}^3$ ),  $F$  is the radial force of the rubber wheel against the sample (N),  $\omega$  is the rotation (rpm),  $R$  is the radius of the rubber wheel (mm), and  $t$  is the elapsed testing time.

### Jet Erosion Test

In jet erosion test (ASTM G73-10), a sample is abraded by repeated impacts of water jets until the degradation/destruction of the coating. The jet erosion apparatus (Fig. 5a, CM4 Enginierya S.L., Barcelona, ES) in CPT facilities consists of two water jets and a central rotating arm (Fig. 5b) that can reach high rotation speed. At the end of the arm, a sample holder keeps the sample parallel to the water jets. The water jets diameter is 4 mm and the process parameters are water pressure (variable from 0.1 to 2.0 Bar), rotation speed (variable from 50 Km/h up to 350 Km/h) and test time. The experiments were carried out at 190 Km/h, with the pressure of water set up at 1 Bar, controlling every 30/60 minutes the sample to measure the weight loss and the damaged area. The test was repeated 3 times for each sample.

**Table 5** Ball on disk parameters

Diameter of path	Ball	Rotation	Sliding speed	Sliding distance	Number of cycles
14 mm	WC-Co diameter 11 mm	124 rpm	0.13 m s <sup>-1</sup>	999.5 m	22737

**Table 6** Rubber wheel testing parameters

Rubber wheel rotation	Rubber wheel peripheral velocity	Load	Interval for mass measurement (elapsed time)	Total time
139 rpm	1.66 m.s <sup>-1</sup>	125 N	15 s (0–60 s) 30 s (60–300 s) 60 s (300–600 s) 300 s (600–1800 s)	1800 s

**Fig. 4** (a) Scheme and (b) Equipment for the rubber wheel testing, (1) Abrasive feeder, (2) Rubber wheel diameter 9 in (228.6 mm), (3) Controller, (4) Used abrasive container, (5) Load, (6) Sample and (7) Rotation of the wheel

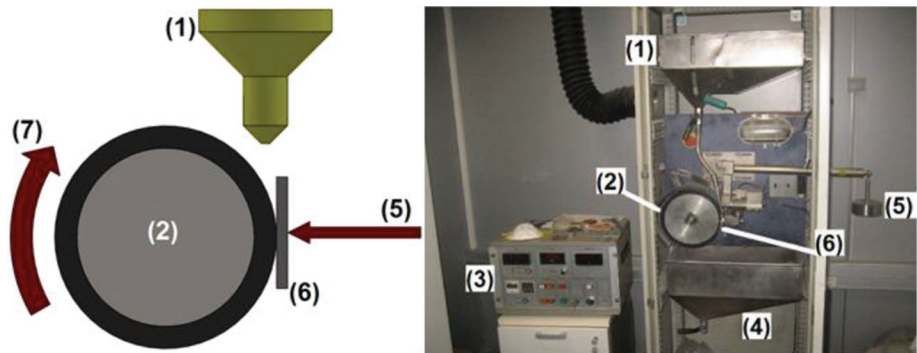


**Fig. 5** Jet erosion equipment (a) and central rotating arm (b)



**Result and Discussion**

**Powders Properties**

Figure 6 depicts the SEM microstructure of the starting feedstock powders used in this investigation. Particles have a quasi-spherical shape due to the employed gas atomization production process (Ref 28); some particles show the presence of satellites (Ref 31). The particles size distribution is shown in Fig. 7. A narrow size distribution can be

underlined. XRD confirmed that the crystallographic structure of the starting powders is the FCC phase (Fig. 8) (Ref 30) (Fig. 8).

As demonstrated in (Ref 33), powders flow rate is a fundamental characteristic for the cold spray process because an increase in flowability of the powders leads to an increase in deposition efficiency of the process. It is well-known that powders with spherical shape have a higher flowability than irregular ones and for this alloy. The

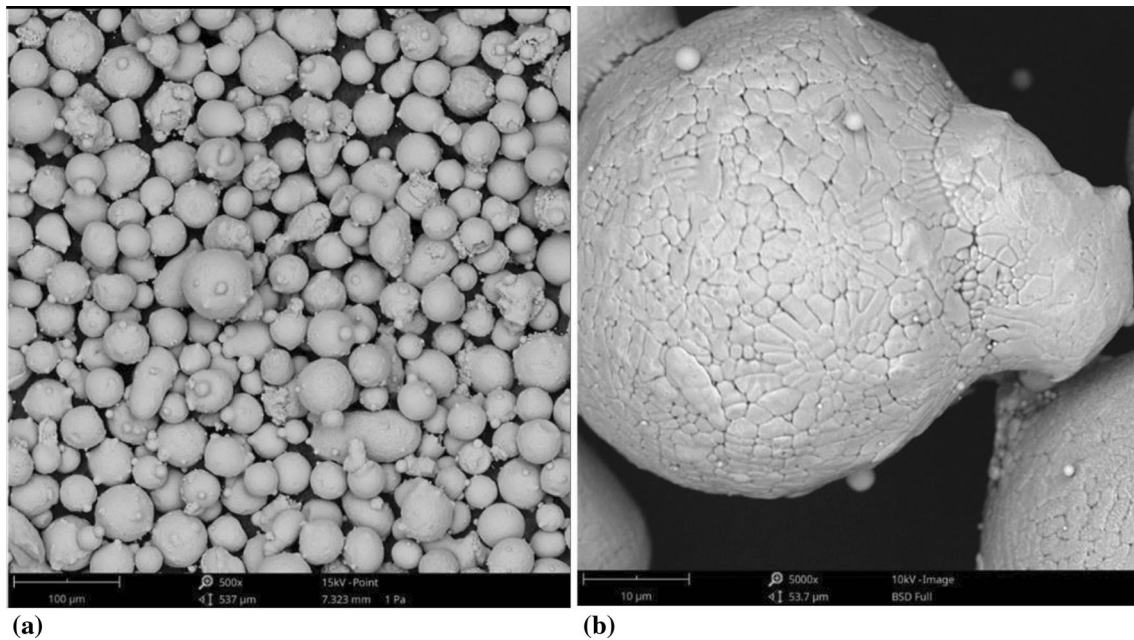
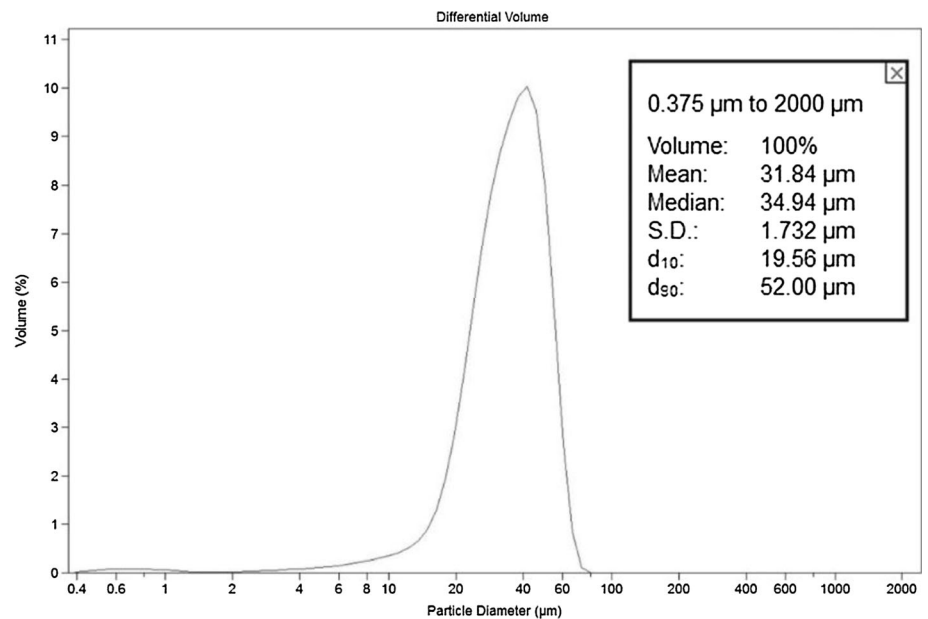


**Fig. 6** SEM free surface of FeCrCoMnNi powders (a) and high magnification of a particle (b)

**Fig. 7** Particles distribution size



medium value of flowability for the mean particles size and the measured density is shown in Table 7.

Besides, splat tests were carried out to investigate not only the influence of substrate material on particles deformability, but also the coating/substrate interaction. In Fig. 9(a), a splatted cold-sprayed particle is shown; in Fig. 9(b), the splatted HVOF one can be observed. If in (Ref 30) the cold-sprayed particle is surrounded and locked by the aluminum substrate, in this case, the particle cannot penetrate entirely the C-Steel substrate, due to its hardness. Despite this aspect and even if the deformation at the top of

the particle is limited, it can be confirmed the severe plastic deformation of downside of the cold-sprayed particles. In the case of the HVOF splat test, the particle is well-melted, and it is well-known that thanks to the impinging of the molten particles, the formed coatings will have a lamellar microstructure. The growth of this lamellar microstructure depends on particles size, process parameters as well as in-flight particles velocity (Ref 34).

The nanohardness of the particles was measured on the cross-section surfaces (Fig. 10a). The obtained values of nanohardness and elastic modulus are  $1.5 \pm 0.17$  GPa and

**Fig. 8** XRD pattern of the as received HEAs particles

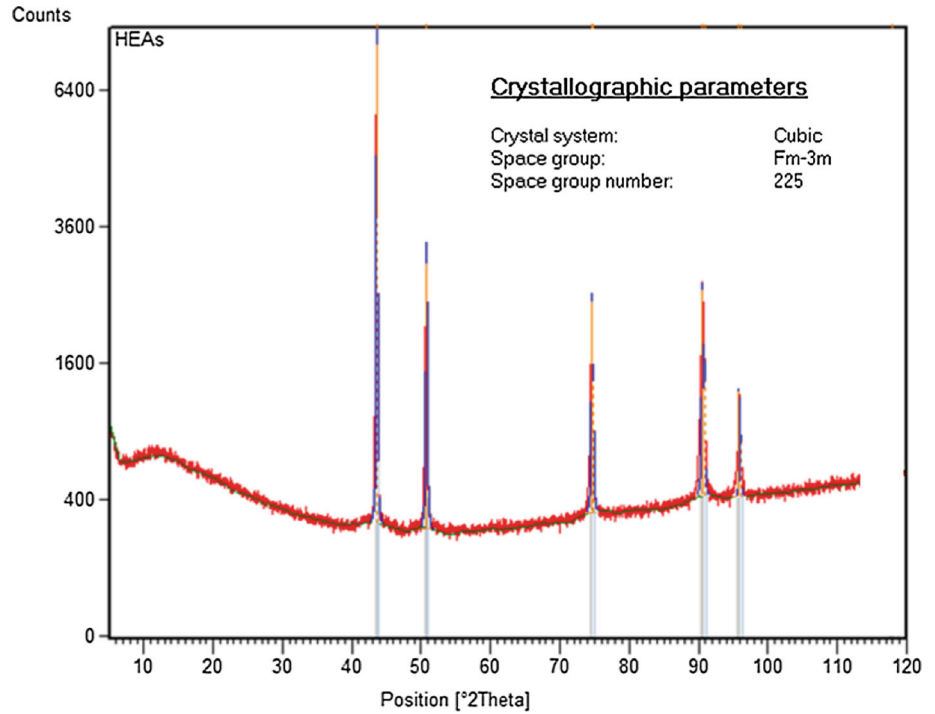
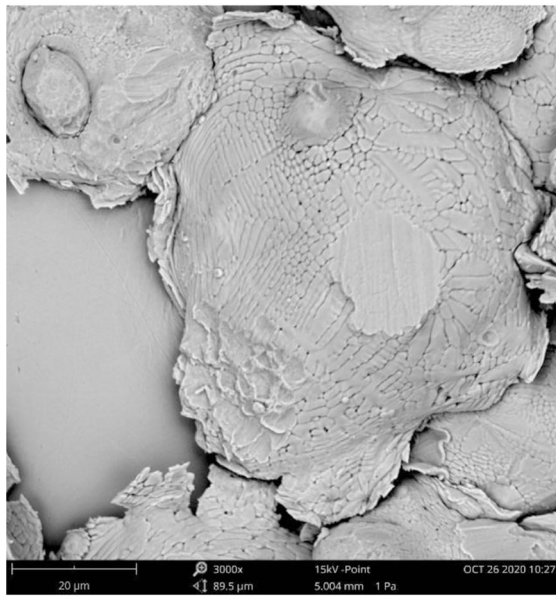
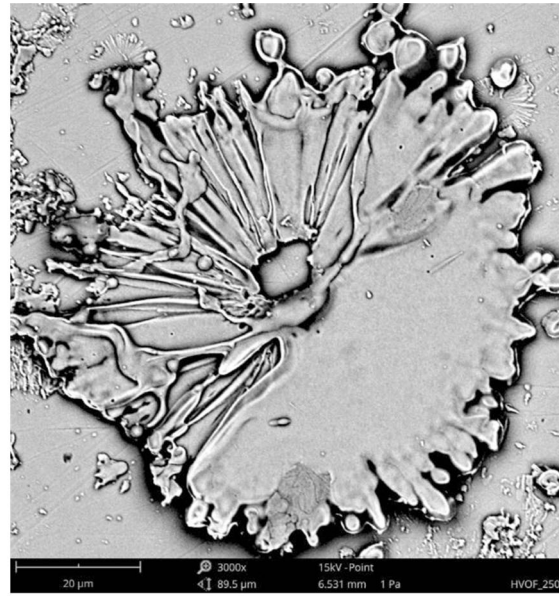


**Table 7** Particles distribution, apparent density and flow rate of the FeCoCrMnNi powders

Particle size distribution ( $\mu\text{m}$ )	Apparent density ( $\text{g cm}^{-3}$ )	Flow rate ( $\text{g s}^{-1}$ )
Mean 34.94	$4.44 \pm 0.02$	$3.04 \pm 0.02$



(a)



(b)

**Fig. 9** Splat tests of CGS<sub>N2</sub> (a), HVOF<sub>250</sub> (b)

$130 \pm 3.5$  GPa, respectively. Using the equation to convert the nanohardness measured with a Berkovich indenter into a Vickers hardness (HV) as in (Ref 35), the obtained value is 139 HV and the ultimate tensile strength is 460 MPa. To

explain the difference between these values and those in (Ref 35), it should be taken into account the different applied loads. The used Poisson ratio was 0.29, which is the same as the stainless steel and as underlined in (Ref



36), the most important aspect is that in the plastic region Cantor alloy is stronger than a single Ni particle because in HEAs alloys, each element is represented in the same quantity and so that, each element plays the same role in lattice distortion. Even if the obtained results in terms of nanohardness and elastic modulus are lower than other HEAs (Ref 37, 38), it was shown how the Cantor alloy behavior could be compared to stainless steel.

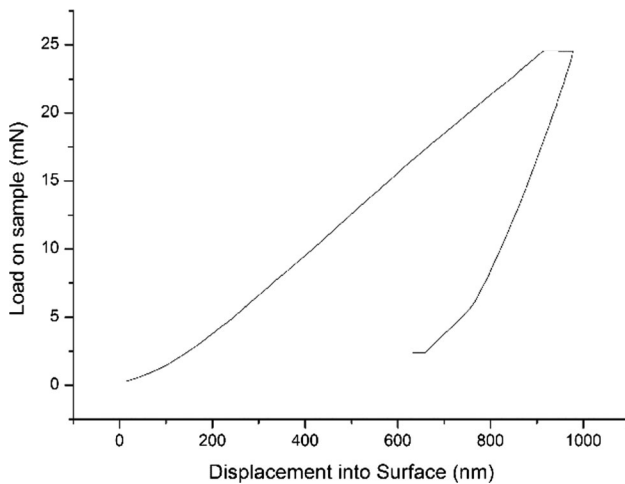


**Fig. 10** Load–displacement curve

**Table 8** Cold-sprayed coatings optimization

Pressure (MPa)	Temperature (°C)	SOD (mm)	Thickness (μm)	Porosity (%)	DE (%)
50	1000	30	237 +/-37	8	52
60	1000	30	382 +/- 28	3	65
70	1100	30	...	...	...
70	1100	15	593 +/- 31	<1	87

## Coatings Deposition

The optimization of cold spray and HVOF coatings was carried out by varying not only carrier gas pressure and temperature, but also the stand-off distance between the gun and the substrate. The followed procedure was to detect the coatings porosity and the deposition efficiency as a function of the tuned processing parameters. They were chosen because in our previous experiences the coatings properties are very sensitive to the variation of the selected parameters (Ref 39, 40). To obtain thick and dense cold-sprayed coatings, the tested gas pressures were 5 MPa, 6 MPa, and 7 MPa, while the temperatures were 1000 °C and 1100 °C (Table 8).

In Fig. 11(a), we can see the coating deposited at 5 MPa-1000 °C coating, while in Fig. 11(b), the one deposited at 6 MPa-1000 °C one, both were sprayed at 30 mm of SOD.

As demonstrated in (Ref 24, 41-45), the increase in carrier gas temperature and pressure leads to an increase in particles in-flight velocity and consequently, to an increase in deposition efficiency as well as a decrease in porosity. Based on our previous experience with Inconel 625 (Ref 44) and also with stainless steel (Ref 45), the higher pressure and temperature, the better results on density and DE. Also, previous papers on HEAs deposited using cold spray process (Ref 30, 32) are used to set starting process parameters and to carry on the optimization process. The

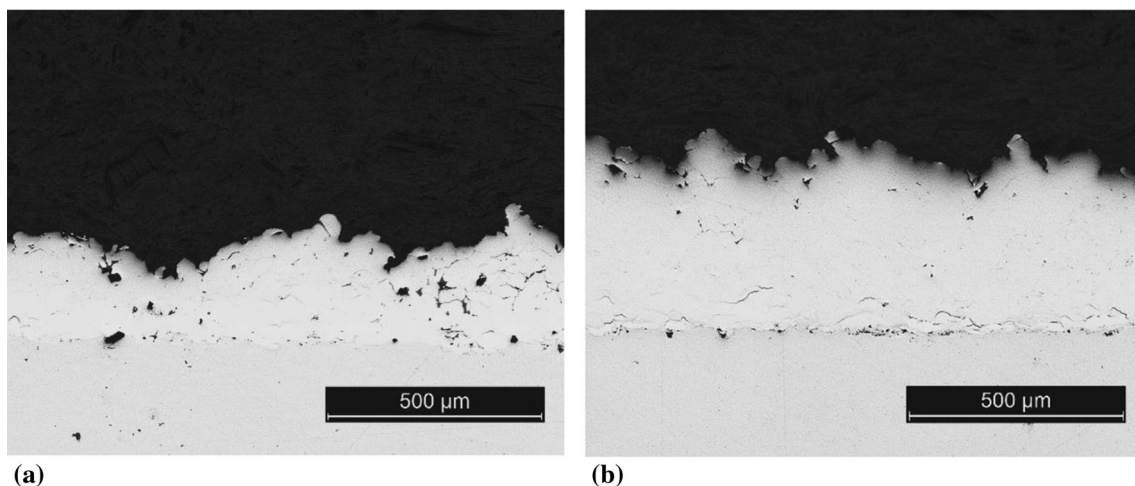


**Fig. 11** 5MPa-1000 °C coating (a) and 6MPa-1000 °C coating (b)

coating deposited at 7 MPa–1100 °C and 30 mm of SOD showed a de-cohesive behavior; this was attributed to the higher temperature of in-flight particles.

The higher thermal input transferred to the particles reduces their deformation strain at impact, what can cause a loose of cohesive strength, resulting in higher strain produced at lower temperature. In these spraying conditions, the previous layer of deposited particles does not deform enough during the impact, leading to a non-optimal cohesion between the different layers. The microstructure of the optimized coating sprayed at 7 MPa and 1100 °C and 15 mm SOD is shown in Fig. 12. In general terms, it is well-known that the bow shock effect depends on standoff distance and, as a result of a reduction in particle velocity, it has a negative influence on deposition efficiency. Near the substrate, the bow shock effect causes a strong increase

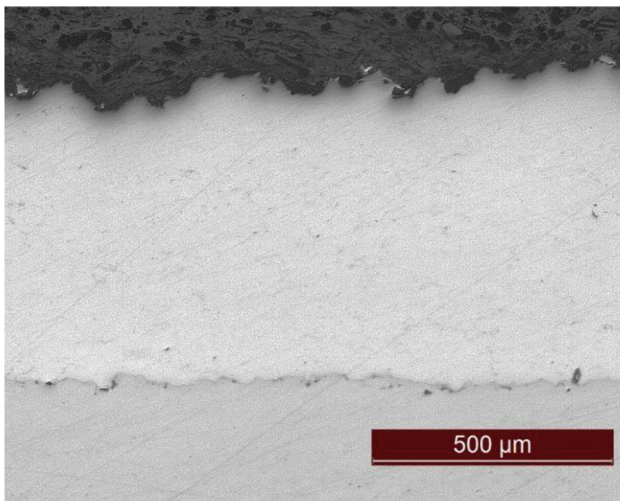


**Fig. 12** HEA coating cold sprayed at 7MPa-1100 °C and 15 SOD

in the turbulent kinetic energy and for this reason, the particles are slowed down. Obviously, smaller particles are more affected than bigger ones. For example, smaller particles behavior is like a dust that does not impact on the substrate at all or is too slow for bonding. Thus, the bow shock effect on the particles velocity is related to the particles size, density and shape (Ref 46–49). In our study, even if we have sprayed at a short standoff distance, the bow shock effect is mitigated from the particle density and size because the specific weight of Cantor alloy is similar to that of another material previously sprayed from the authors (Ref 50) at SOD of 10 mm and median particles size is close to 35 μm. It is well-known that the density of the cold-sprayed coatings depends on process parameters, as well as the shape and the size distribution of the starting powders (Ref 46). Even if in (Ref 47) is reported that porosity increases with increasing the powder d10 value, in this case, a less than 1% porosity level is reached thanks to the high flattening of sprayed particles. It is worth remembering that this porosity level is evaluated as a mean value of seven images.

The aspect of the coatings deposited through HVOF in different conditions is shown in Fig. 13, while Table 9 shows the process parameters used. They were chosen because of our previous experience with other materials, such as Ni-based superalloys and stainless steel (Ref 53). To improve the quality of the coatings, the focus was on SOD distance using already known process conditions (Ref 54).

Figure 14 shows the etched aspect of the cold-sprayed and HVOF coating deposited using the optimized process conditions. The etching reveals the particle boundaries, the dendritic microstructure as well as the deformation and the width and height of individual splats. In the case of cold-sprayed coating, it is well-shown the deformation and the

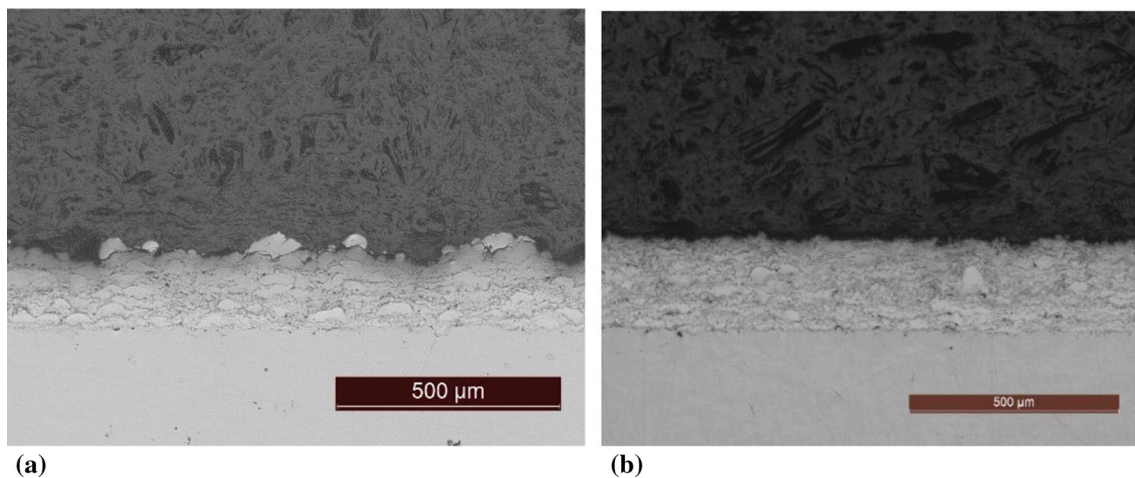


**Fig. 13** HVOF\_225 (a) and optimized HVOF\_250 coating (b)

pancake-like shape of the particles, and the image can be used to definite the flattening ratio (Ref 46, 49), considering the larger over the smaller particle dimension of the splatted particle.

### Mechanical and Corrosion Properties

The XRD pattern of the CS and HVOF optimized coatings is shown in Fig. 15; for comparison, the results belonging to the as-received particles are provided. As mentioned above, the peaks of as-received particles are characteristic of FCC structure. As expected, cold-sprayed coating shows

no phase change, while in the case of HVOF coating, there are new peaks. In particular, in Fig. 16, the high magnification resolution shows that those peaks belong to iron oxide and manganese-chrome oxide formation.

Based on XRD analysis, the cooling rate in the case of HVOF process does not affect the HEAs structure because it retained the starting FCC structure. Even if Fig. 16 shows a certain degree of oxidation, there is no shifting of main peaks, and so the dynamic amorphization process is avoided (Ref 56).

The nanoindentations performed on the optimized coatings are shown in Fig. 17. The hardness value of

**Table 9** HVOF process parameters

Coating	H <sub>2</sub> Flow rate	O <sub>2</sub> Flow rate	Air Flow rate	Powder feed	Standoff distance	Robot speed	Step	Number of layers
HVOF 225	12 l/s	2.45 l/s	6.5	0.50 g/s	225 mm	500 mm/s	5 mm	10
HVOF_250	10.6 l/s	3.6 l/s	5.7 l/s	0.50 g/s	250 mm	500 mm/s	5 mm	10

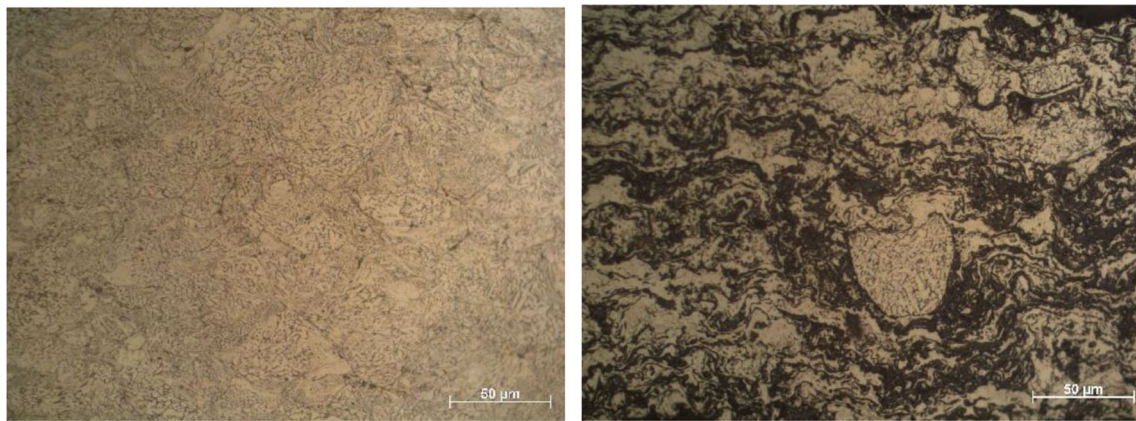


**Fig. 14** Etching of CGS\_N2 (a) and HVOF\_250 coatings (b)

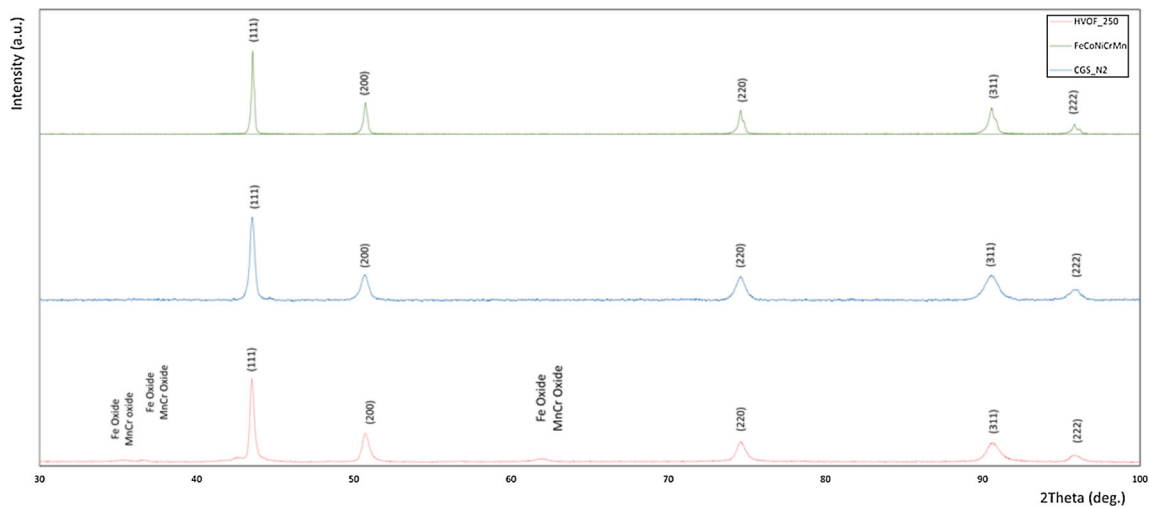


**Fig. 15** XRD of different coatings

**Fig. 16** High magnification of XRD HVOF

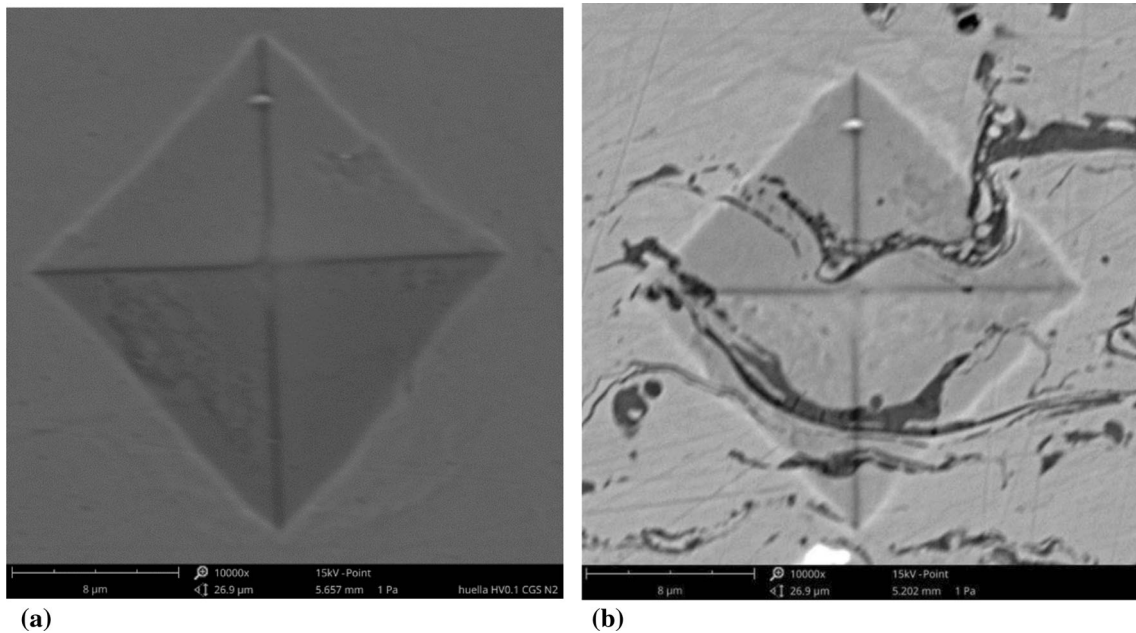
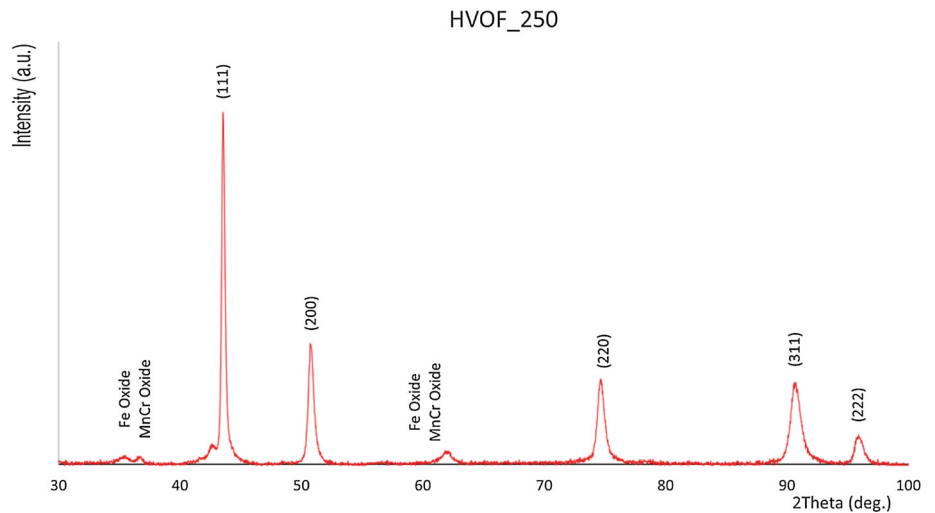


**Fig. 17** High magnification indents of CGS\_N2 (a) and HVOF\_250 (b)

HVOF coating is a slightly greater ( $390 \pm 10 \text{ Hv}_{0.1}$ ) than the hardness value of cold-sprayed coating ( $382 \pm 6 \text{ Hv}_{0.1}$ ). These similar values are due not only to the very low porosity level of both coatings, but also to the new phase formation (Ref 57, 58) during HVOF deposition process (Fig. 16). These oxides make comparable the hardness of HVOF coatings to the hardness obtained thanks to the high plastic deformation and the work-hardening structure of the cold spray process (Ref 59, 60). According to (Ref 46), also powders morphology affects hardness because irregular shape leads to higher hardness values, thanks to a greater defect density. For comparison, the hardness value of 316L and C steel bulks are  $300 \pm 18 \text{ Hv}_{0.1}$  and  $220 \pm 17 \text{ Hv}_{0.1}$ , respectively.

**Table 10** Coatings characterization

	Adhesion strength (MPa)	Hv0.1
CGS_N <sub>2</sub>	27±5	382 ± 6.0
HVOF_250	25±5	390 ± 10.0
316L Bulk	...	300 ± 18.0
C_Steel_Bulk	...	220 ± 17.0

All the obtained results are summarized in Table 10 along with the indication of the measured adhesion strength of the optimized coatings. In (Ref 60), the authors clearly defined the three different formation mechanisms of the

bonding at the coating/substrate interface. Even if in this case the intermixing phenomenon is not plainly visible due to the substrate hardness, the adhesion strength value is reached thanks to the severe plastic deformation of particles that generate mechanical interlocking. In the case of coatings sprayed at 1100 °C and a standoff distance of 30 mm, the in-flight thermal softening of the particles could be the reason for low adhesion strength. To avoid this issue, the standoff distance was reduced, increasing the particle impact effect on the substrate and on the layer previously deposited. For this reason, the results reached at 7MPa-1100 °C and a stand-off distance of 15mm, due to the greater plastic deformation of the particles, are better than those reached applying the same condition but at a stand-off distance of 30 mm.

Table 11 shows not only the corrosion potential and the corrosion current values of the two optimized coatings, but also those of the C-Steel and 316L bulks used to carry out the benchmark. Both the cold-sprayed and HVOF coatings protect the C-Steel substrate, improving significantly its performance because they well impede the path of the electrolyte to the substrate due to their very low porosity levels. In general, the cold-sprayed coatings show higher  $E_{\text{corr}}$  and higher  $I_{\text{corr}}$  than HVOF coatings, due to the differences of the microstructure. Probably, in the case of cold-sprayed coatings, the  $I_{\text{corr}}$  finds the path through the grain boundaries of the deformed particles. Taking into account the results shown in Table 11, we can classify from high-to-low  $E_{\text{corr}}$  as follows (Fig. 18): CGS\_N<sub>2</sub>, 316L\_Bulk, HVOF\_250 and C\_Steel\_Bulk. These results are explained by the Cr and Ni content percentage (20% for HEAs, 17 and 12%, respectively, for 316L\_Bulk) and by the oxidation of HVOF deposition process. As demonstrated above by XRD analysis, the presence of cobalt oxide and Fe oxide slightly worsen the  $E_{\text{corr}}$  performance of the HVOF coatings. Thanks to its intrinsic properties, the 316 bulk sample exhibited better  $I_{\text{corr}}$  resistance, followed by the cold-sprayed and HVOF coatings. Supposing that these coatings would be work as a protective layer between the environment and the substrate, the results reached are encouraging.

**Table 11** Corrosion potential and current

	E (mV)	I (μA)
316L BULK	– 195	0.04
C STEEL BULK	– 730	0.50
CGS_N <sub>2</sub>	– 65	1.20
HVOF_250	– 440	0.29

The coefficient of friction between a WC-Co ball and both the coatings and the bulks was measured through the ball-on-disk test. Figure 19 presents the evolution of the coefficient of friction that was calculated when the system reached a stationary behavior, after 15.000 cycles. Table 12 shows that the CoF of both coatings is higher than that of both bulks due to wear mechanism.

Figures 20 and 21 show the wear tracks of optimized CGS\_N<sub>2</sub> and HVOF\_250 coatings, respectively, while Figs. 22 and 23 show the occurred oxidation of both optimized coatings through the EDS mappings.

The wear mechanism is adhesive type and Fig. 20(b) and (b) show a large amount of debris rolled, adhered and oxidized on the wear track. This mechanism is more visible in the cold-sprayed coatings, due to lower cohesion strength between the plastic deformed particles in comparison with melted particles of HVOF process. For this reason, to improve the mechanical properties of cold-sprayed coatings, some authors have studied the effects of heat treatments on the coatings after the cold spray deposition (Ref 61–63). Also, Fig. 24(a) and (b) show the width of the wear track for both coatings, and these values are been used to calculate the friction wear rate, as recommended by ASTM G99-04.

After 30 minutes of rubber wheel tests, the wear rate found for both cold-sprayed and HVOF coatings was lower than that of both 316L and carbon steel bulks. The abrasive wear rates obtained after the stabilization of the mass loss were  $1.6 \times 10^{-4}$ ,  $1.8 \times 10^{-4}$ ,  $2.0 \times 10^{-4}$  and  $2.2 \times 10^{-4}$  mm<sup>3</sup>/Nm for samples HVOF\_250, CGS\_N<sub>2</sub>, 316L\_Bulk and C\_Steel\_Bulk, respectively (Table 12). The better performance of HVOF\_250 is due to the formation of hard new phases, as shown by the XRD analysis. The presence of oxides in the HVOF coatings ensures a greater wear resistance than the cohesion of mechanically bounded particles deposited by the cold-sprayed process. It is well-known that the abrasion mechanism causes the removal of the softest material, and the wear resistance of coating depends on its porosity, hardness and composition (Ref 50). Besides, the thermal-sprayed coatings showed a better wear rate compared to both bulks due to the different values of surface roughness, because in the case of the coatings, it was higher than that substrates. In addition, the SiO<sub>2</sub> sand abrasive particles have a larger size ( $\approx 200 \mu\text{m}$ ) compared to the size of HEAs particles in the coatings, as was revealed by the chemical etching (Fig. 14). As demonstrated in (Ref 51), this means that the pressure generated between the sand particles and the coatings pulls out the HEAs particles from the coating. This “pull out” mechanism (see the rounded black holes in Fig. 25(a) and (b)), combined with the higher hardness of the coatings, allows for less material loss than the plastic deformation mechanism observed for a substrate without coating (Ref

Fig. 18 Polarization curves

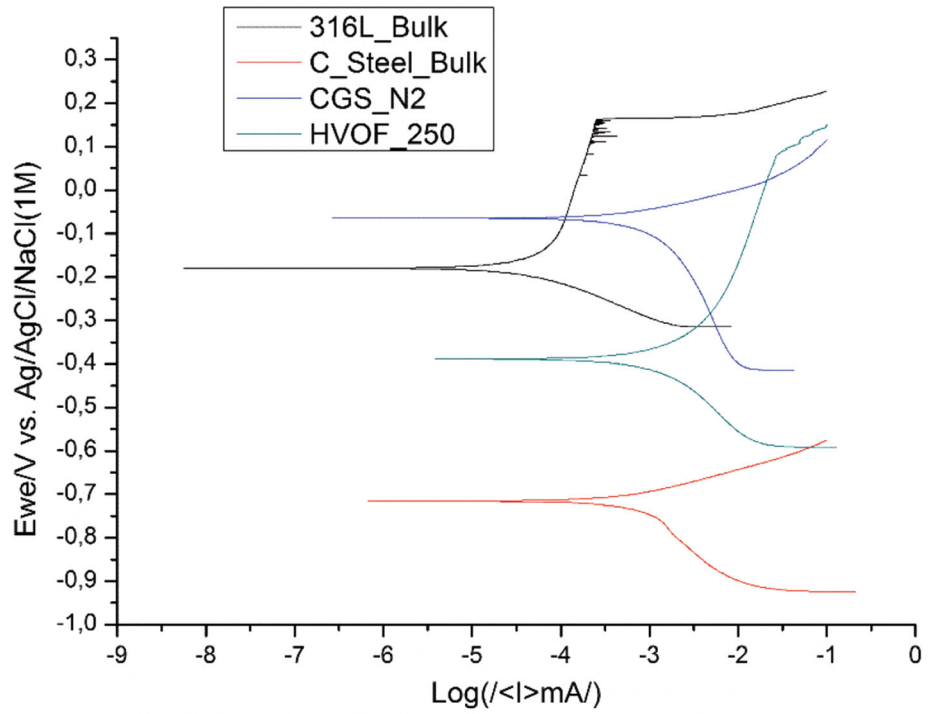


Fig. 19 CoF—ball on disk

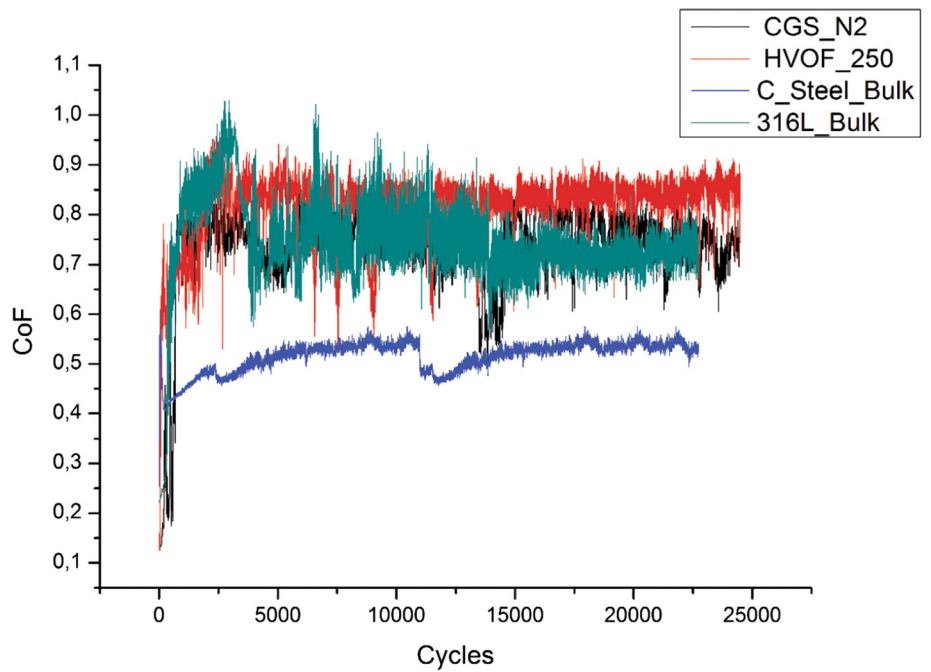
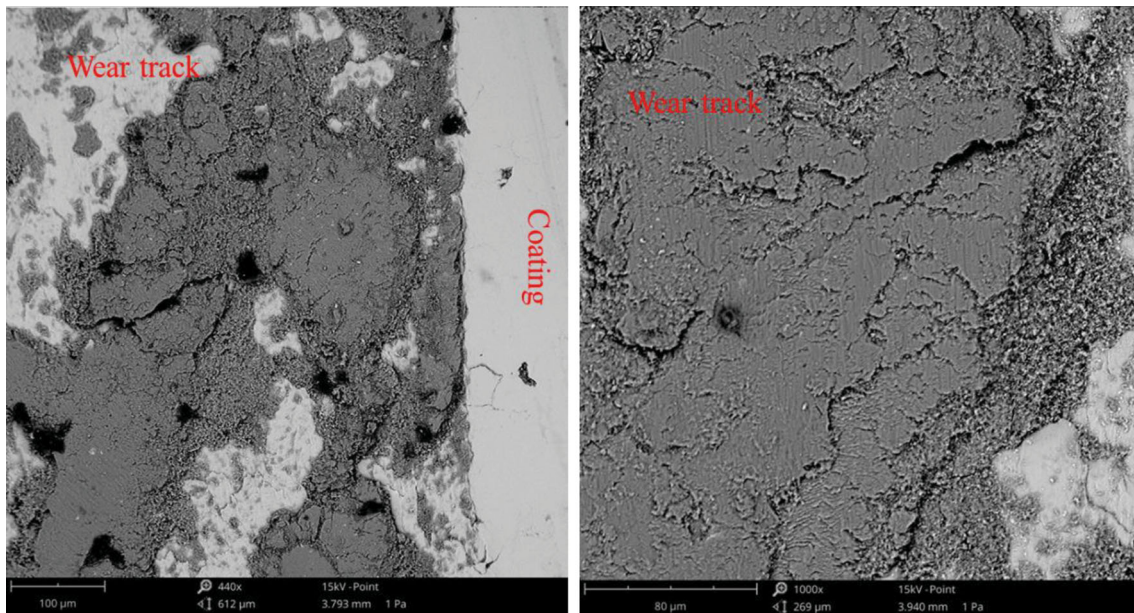
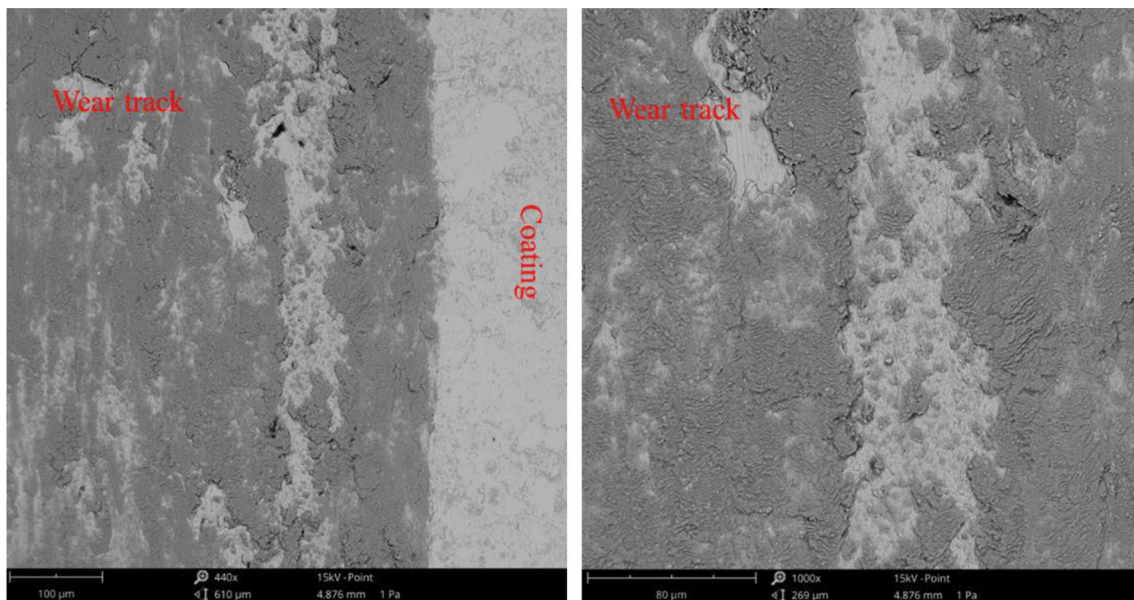


Table 12 Wear behavior

	Abrasion rate ( $\text{mm}^3 \text{N}^{-1} \text{m}^{-1}$ )	CoF	Friction wear rate ( $\text{mm}^3 \text{N}^{-1} \text{m}^{-1}$ )
316L BULK	$2.0 \times 10^{-4} \pm 7.0 \times 10^{-5}$	$0.65 \pm 0.08$	$1.69 \times 10^{-4}$
C STEEL BULK	$2.2 \times 10^{-4} \pm 6.5 \times 10^{-5}$	$0.53 \pm 0.01$	$3.06 \times 10^{-5}$
CGS_N <sub>2</sub>	$1.8 \times 10^{-4} \pm 5.3 \times 10^{-5}$	$0.73 \pm 0.04$	$2.80 \times 10^{-4}$
HVOF_250	$1.6 \times 10^{-4} \pm 5.6 \times 10^{-5}$	$0.81 \pm 0.11$	$6.70 \times 10^{-5}$



**Fig. 20** (a) Wear track on CGS\_N2 coating and (b) High magnification



**Fig. 21** (a) Wear track on HVOF coating and (b) High magnification

51). Thereby, both coatings improved the abrasive wear properties of the substrates (Fig. 26).

The erosion by water droplets impact is another crucial wear mechanism for different industrial sectors such as

wind turbine blades, powerplant, and aeronautic applications (Ref 51-53). According to ASTM G73-10, the water jet erosion mechanism is the same observed during cavitation erosion tests, and the ideal case study shows that the

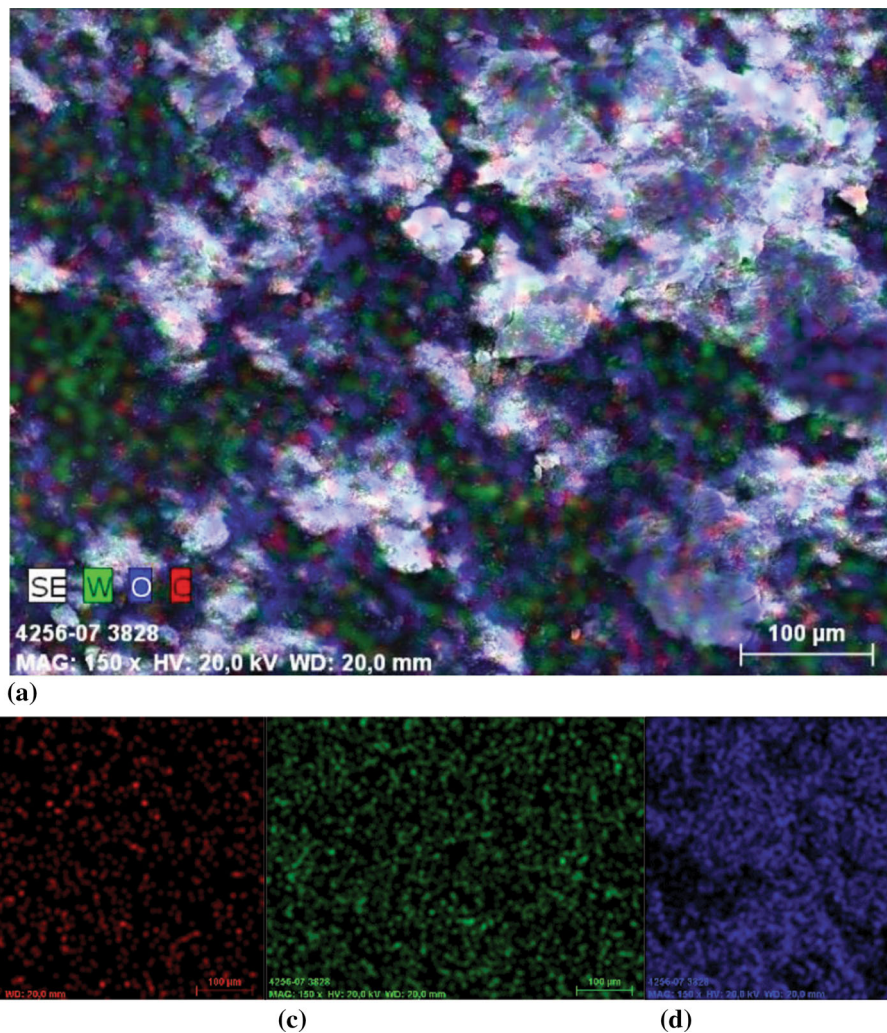


**Fig. 22** EDS mapping of (a) CGS\_N2 coating and (b) C, (c) W, (e) O

erosion slopes usually divide into three zones. The first zone is the so-called incubation zone, in which there is no material erosion; the second zone is characterized by the acceleration of erosion rate up to a maximum value and finally, the third zone shows a steady-state mass lost rate. As reported in (Ref 53-55) for other thermally sprayed coatings, also in our investigation in no case the incubation stage was observed (see Fig. 27), due to the brittle of both coatings and both bulks. Between the tested materials, the 316L bulk has better erosion resistance, while the CGS\_N2

coating is the worse. The poor erosion resistance of cold-sprayed coating could be explained looking at Fig. 28, where the SEM image of droplets impact zone is shown. The continuous and prolonged impact of the water rips away the rounded particles that are not melted as in the case of HVOF deposition process. Here too, the erosion resistance of cold-sprayed coatings depends on the cohesion strength between the particles, which is not enough to resist the liquid impingement. In the case of C steel bulk, it is shown how it well-resists during the initial stage of the



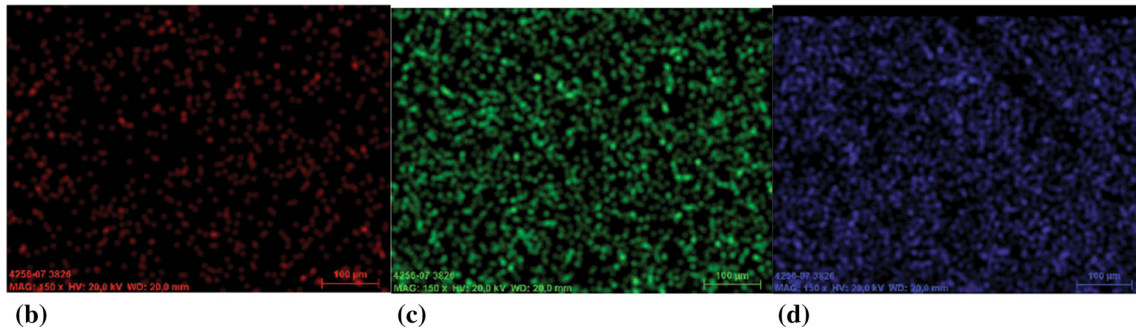
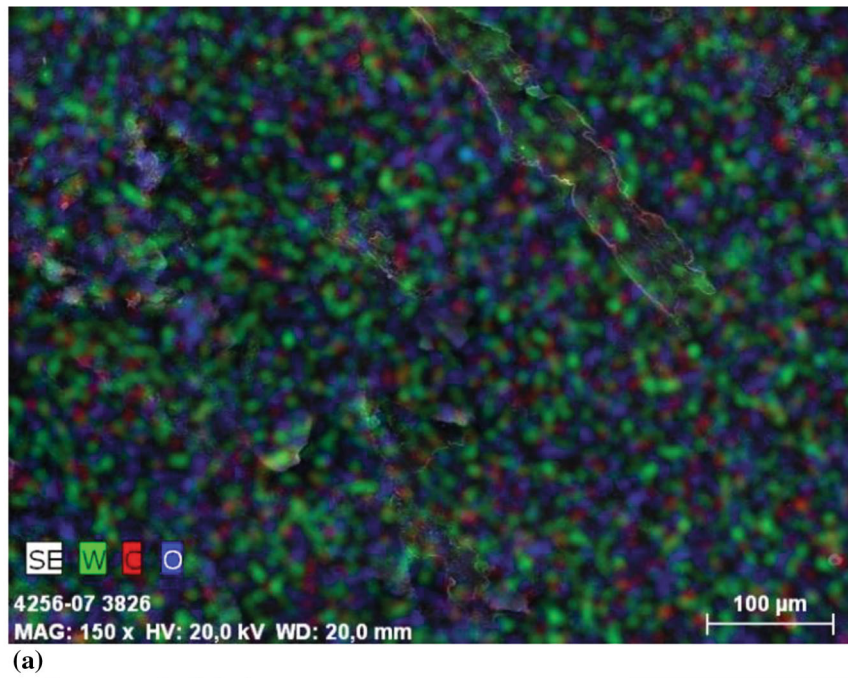


**Fig. 23** EDS mapping of (a) HVOF\_250 coating and (b) C, (c) W, (e) O

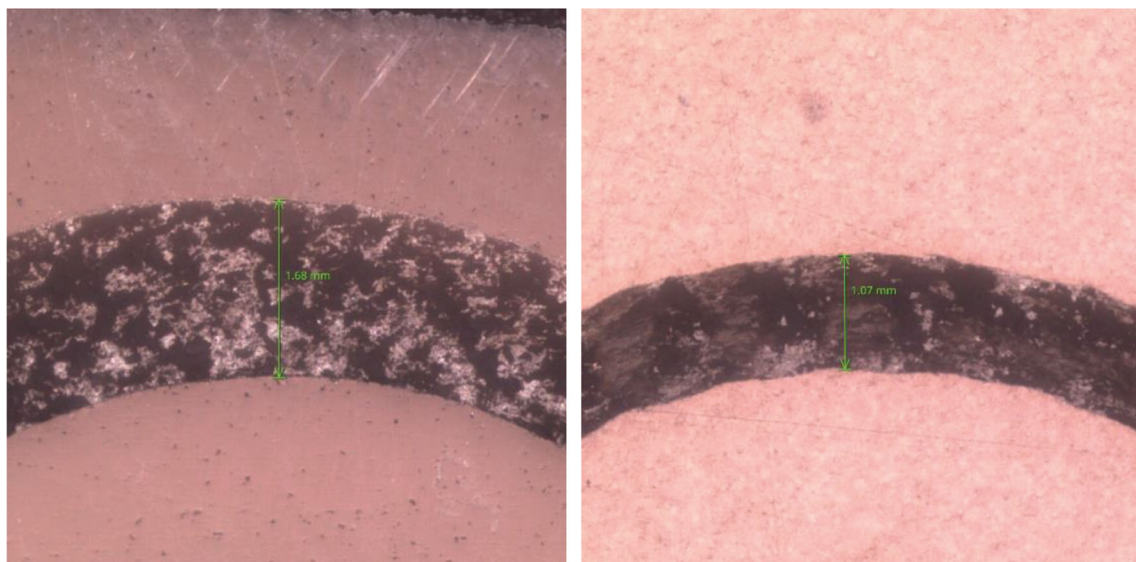


**Fig. 24** Wear track width of (a) CGS\_N2 coating and (b) HVOF\_250 coating used for friction wear rate

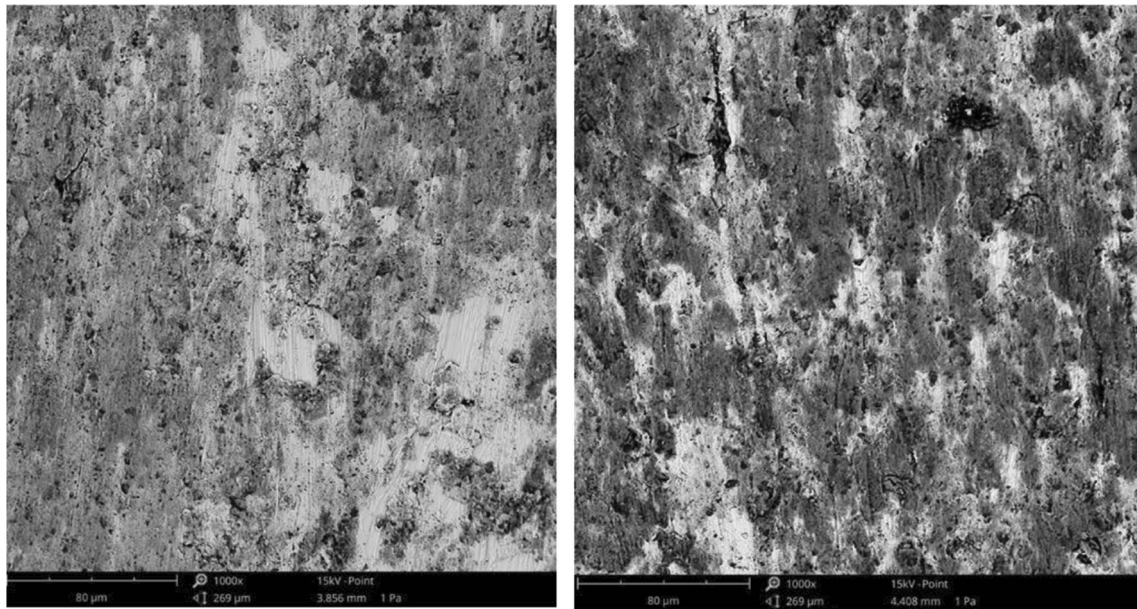
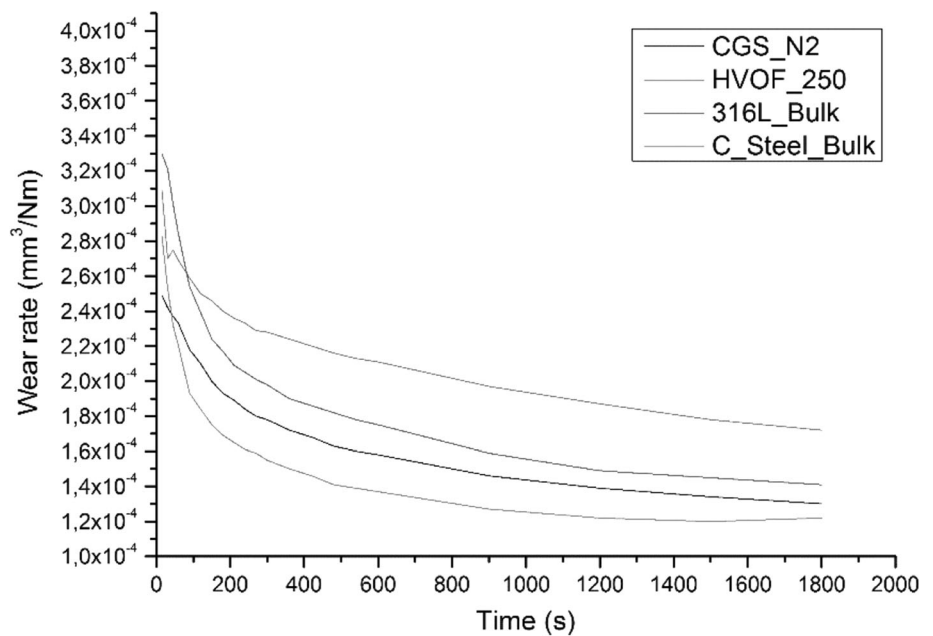


**Fig. 25** SEM images of (a) CGS\_N2 and (b) HVOF\_250 rubber wheel wear track

**Fig. 26** Wear rate and rubber wheel



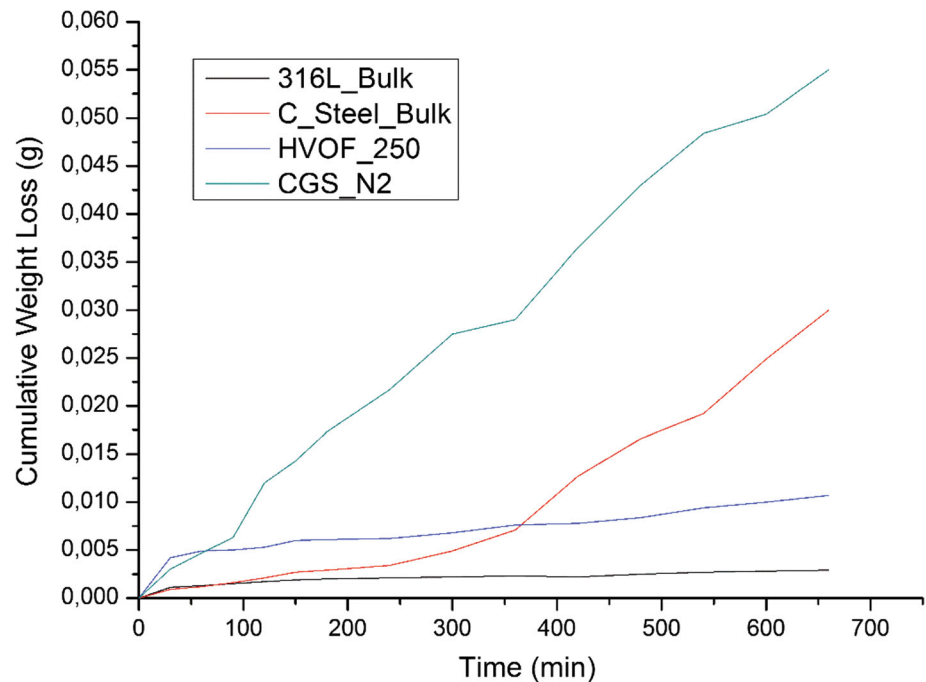
test but after 350 minutes, and it is well-visible to the change of the slope. This is due not only to the erosion mechanism, but also to the corrosion of the hitting zone.

**Conclusion**

- A complete HEAs starting powders characterization was carried out, in terms of size, shape, flow rate,

density, microstructure, and nanohardness. In particular, obtained nanohardness results showed a behavior similar to stainless steel.

- Dense and thick Cantor alloy coatings were obtained onto a C steel substrate by cold spray and HVOF processes. The microstructural and the mechanical characterization of coatings were carried out, and their wear resistance was investigated. In the case of cold spray process, coatings optimization has been

**Fig. 27** Jet erosion test results

performed starting from 5 MPa-1000 °C, 6MPa-1000 °C, and 7MPa-1100 °C, stand-off distance 30 mm. It was clear that at 5 MPa pressure, the quality of the coating is poorer, and the deposition efficiency is smaller. There is a clear trend of decreasing porosity and increasing deposition efficiency when raising up the pressure and the temperature, being better at 7 MPa and 1100 °C, but then there was a problem with adhesion. The thermal softening of the particle when increasing temperature up to 1100 °C at 30 mm could be the reason for decreasing adhesion, and that is why the distance was reduced in this case to increase the particle impact effect on the substrate and solve that problem. The best results have been obtained at 7MPa-1100 °C and a stand-off distance of 15mm due to the greater plastic deformation of the particles. Under the same conditions but at a stand-off distance of 30 mm, the particles partially melt in flight, so that when they reach the substrate, the plastic deformation level is lower. For the cold-sprayed optimum conditions, a deposition efficiency of 87% is obtained. The thickness measured for a two-layer cold spray coating was

593±31 μm, and for a ten-layer HVOF coating was 210±20 μm. Both obtained coatings showed very low porosity <1%.

- As expected, no phase changes are observed using the cold spray process, while the formation of Fe and MnCr oxides is visible in HVOF coatings. The presence of these oxides leads to a hardness value similar for both process deposition. A hardness of (382±6) HV0,1 has been measured for the CS coating and a value of (390±10) HV0,1 for the coating deposited by HVOF. These values are very similar taking into account that using the CS technique no oxides are obtained. For the HVOF coatings, oxides provide an increase in surface hardness and better wear resistance. It could be useful to underline that in the case of HVOF process, the obtained results depend strictly on torch used. Other HVOF equipment may produce coatings of different quality.
- The dense cold-sprayed coating does not allow the path of the electrolyte toward the substrate, and its Ecorr value depends on the high Cr and Ni content. For the

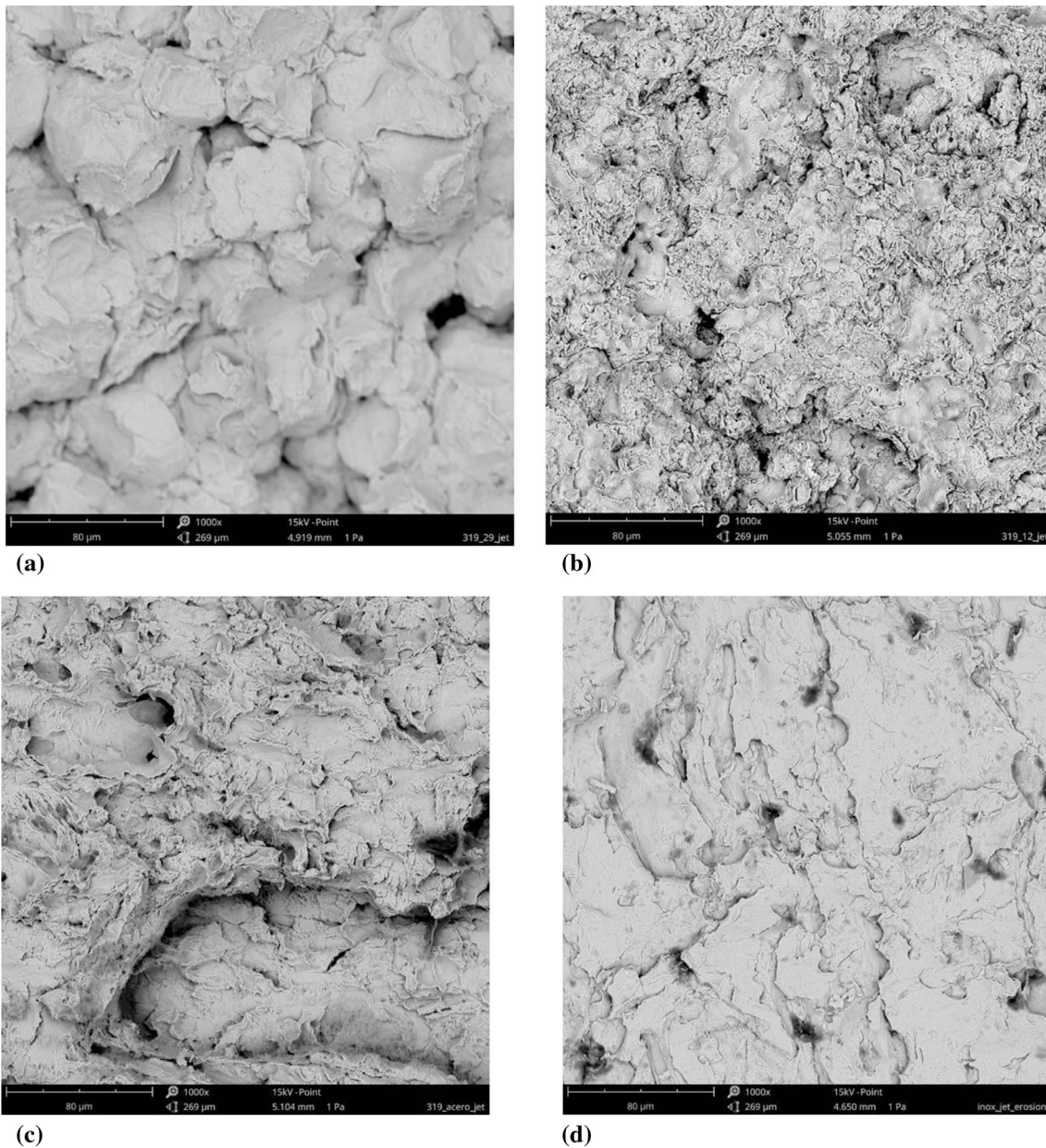


**Fig. 28** Jet erosion impact zone SEM image of (a) CGS\_N2, (b) HVOF\_250, (c) C\_Steel\_Bulk and (d) 316L\_bulk

HVOF coating, the presence of the oxides slightly worsed the Icorr value.

- In the case of the rubber wheel, both tested coatings showed very similar values, due to the similar surface

hardness. HVOF coating suffered less wear than cold-sprayed one.

- Due to its molten particles, the ball on disk test for the HVOF coating showed a lower wear rate than the cold-

sprayed one. The HVOF particles are characterized by higher cohesive strength than cold-sprayed particles, and the WC-ball has more difficulty pulling them out.

- In the jet erosion test, the HVOF coating and the 316L bulk showed the same trend, even if the starting behavior is different due to the different surface roughness. The C-steel bulk showed a good erosion resistance in the initial stage of the test, but its wear rate worsening due to the combined erosion and corrosion effect. For the cold-sprayed coating, it has been observed the same behavior of rubber wheel test, due to poor cohesion strength between the particles.
- Both cold-sprayed and HVOF Cantor alloy coatings protected the substrate, although not in the same way. The cold-sprayed coating was effective in increasing corrosion resistance, but it did not withstand erosion. By contrast, HVOF coating performed well in all tests, including erosion tests, due to its molten particles.

## References

1. F.Y. Shu, S. Liu, H.Y. Zhao, W.X. He, S.H. Sui, J. Zhang, P. He and B.S. Xu, Structure and High-Temperature Property of Amorphous Composite Coating Synthesized by Laser Cladding FeCrCoNiSiB High-Entropy Alloy Powder, *J. Alloys Compd.*, 2018, **731**, p 662–666. <https://doi.org/10.1016/j.jallcom.2017.08.248>
2. G. Qin, W. Xue, R. Chen, H. Zheng, L. Wang, Y. Su, H. Ding, J. Guo and H. Fu, Grain Refinement and FCC Phase Formation in AlCoCrFeNi High Entropy Alloys by the Addition of Carbon, *Materialia*, 2018, **2019**(6), 100259. <https://doi.org/10.1016/j.mtla.2019.100259>
3. J.-W. Yeh, S.-K. Chen, S.-J. Lin, J.-Y. Gan, T.-S. Chin, T.-T. Shun, C.-H. Tsau and S.-Y. Chang, Nanostructured High Entropy Alloys with Multiple Principal Elements: Novel Alloy Design Concepts and Outcomes, *Adv. Eng. Mater.*, 2004 <https://doi.org/10.1002/adem.200300567>
4. B. Cantor, I.T.H. Chang, P. Knight and A.J.B. Vincent, Microstructural Development in Equiatomic Multicomponent Alloys, *Mater. Sci. Eng. A*, 2004, **375–377**, p 213–218. <https://doi.org/10.1016/j.msea.2003.10.257>
5. Y.F. Ye, Q. Wang, J. Lu, C.T. Liu and Y. Yang, High-Entropy Alloy: Challenges and Prospects, *Mater. Today*, 2016, **19**(6), p 349–362. <https://doi.org/10.1016/j.mattod.2015.11.026>
6. Y. Zhang, T.T. Zuo, Z. Tang, M.C. Gao, K.A. Dahmen, P.K. Liaw and Z.P. Lu, Microstructures and Properties of High-Entropy Alloys, *Prog. Mater. Sci.*, 2013, **2014**(61), p 1–93. <https://doi.org/10.1016/j.pmatsci.2013.10.001>
7. Y. Qiu, S. Thomas, M.A. Gibson, H.L. Fraser and N. Birbilis, Corrosion of High Entropy Alloys, *NPJ Mater. Degrad.*, 2017, **1**(1), p 1–17. <https://doi.org/10.1038/s41529-017-0009-y>
8. S. Kumar, M. Kumar and A. Handa, Combating Hot Corrosion of Boiler Tubes—A Study, *Eng. Fail Anal.*, 2018 <https://doi.org/10.1016/j.engfailanal.2018.08.004>
9. M. Oksa, J. Metsäjoki and J. Kärki, Corrosion Testing of Thermal Spray Coatings in a Biomass Co-Firing Power Plant, *Coatings*, 2016, **6**(4), p 65. <https://doi.org/10.3390/coatings6040065>
10. M. Oksa, T. Varis and K. Ruusuvoori, Performance Testing of Iron Based Thermally Sprayed HVOF Coatings in a Biomass-Fired Fluidised Bed Boiler, *Surf. Coatings Technol.*, 2014, **251**, p 191–200. <https://doi.org/10.1016/j.surfcoat.2014.04.025>
11. T.S. Coatings, *Thermal Spray Coating Corrosion Mitigation at Corrosion Mitigation in Biomass Combustion Plant Using* (2020), pp. 1–22
12. H.S. Sidhu, B. Singh Sidhu and S. Prakash, The Role of HVOF Coatings in Improving Hot Corrosion Resistance of ASTM-SA210 GrA1 Steel in the Presence of Na<sub>2</sub>SO<sub>4</sub>-V<sub>2</sub>O<sub>5</sub> Salt Deposits, *Surf. Coatings Technol.*, 2006, **200**(18–19), p 5386–5394. <https://doi.org/10.1016/j.surfcoat.2005.07.008>
13. M. Oksa, S. Tuurna and T. Varis, Increased Lifetime for Biomass and Waste to Energy Power Plant Boilers with HVOF Coatings: High Temperature Corrosion Testing under Chlorine-Containing Molten Salt, *J. Therm. Spray Technol.*, 2013, **22**(5), p 783–796. <https://doi.org/10.1007/s11666-013-9928-5>
14. D.L. Wu, K.V. Dahl, T.L. Christiansen, M. Montgomery and J. Hald, Corrosion Behaviour of Ni and Nickel Aluminide Coatings Exposed in a Biomass Fired Power Plant for Two Years, *Surf. Coatings Technol.*, 2018, **2019**(362), p 355–365. <https://doi.org/10.1016/j.surfcoat.2018.12.129>
15. M. Oksa, P. Auerkari, J. Salonen and T. Varis, Nickel-Based HVOF Coatings Promoting High Temperature Corrosion Resistance of Biomass-Fired Power Plant Boilers, *Fuel Process. Technol.*, 2014, **125**, p 236–245. <https://doi.org/10.1016/j.fuproc.2014.04.006>
16. G. Singh, N. Bala and V. Chawla, High Temperature Oxidation Behaviour of HVOF Thermally Sprayed NiCrAlY Coating on T-91 Boiler Tube Steel, *Mater. Today Proc.*, 2017, **4**(4), p 5259–5265. <https://doi.org/10.1016/j.matpr.2017.05.035>
17. J. Singh, H. Vasudev and S. Singh, Performance of Different Coating Materials against High Temperature Oxidation in Boiler Tubes—A Review, *Mater. Today Proc.*, 2020 <https://doi.org/10.1016/j.matpr.2020.01.156>
18. E. Sadeghi, N. Markocsan, S. Joshi, *Advances in Corrosion-Resistant Thermal Spray Coatings for Renewable Energy Power Plants: Part II—Effect of Environment and Outlook*, vol. 28 (Springer, 2019). <https://doi.org/10.1007/s11666-019-00939-0>
19. V. Katranidis, S. Gu, T.R. Reina, E. Alpay, B. Allcock and S. Kamnis, Experimental Study of High Velocity Oxy-Fuel Sprayed WC-17Co Coatings Applied on Complex Geometries. Part B: Influence of Kinematic Spray Parameters on Microstructure, Phase Composition and Decarburization of the Coatings, *Surf. Coat. Technol.*, 2017, **328**, p 499–512. <https://doi.org/10.1016/j.surfcoat.2017.09.027>
20. V. Katranidis, S. Gu, B. Allcock and S. Kamnis, Experimental Study of High Velocity Oxy-Fuel Sprayed WC-17Co Coatings Applied on Complex Geometries. Part A: Influence of Kinematic Spray Parameters on Thickness, Porosity, Residual Stresses and Microhardness, *Surf. Coat. Technol.*, 2017, **311**, p 206–215. <https://doi.org/10.1016/j.surfcoat.2017.01.015>
21. J. Li, Y. Huang, X. Meng and Y. Xie, A Review on High Entropy Alloys Coatings: Fabrication Process and Property Assessment, *Adv. Eng. Mater.*, 2019 <https://doi.org/10.1002/adem.201900343>
22. R. Cortés, M.Á. Garrido, P. Poza, A. Martos, S. Dosta and I. García, Cold Sprayed Coatings for Repairing Damaged Metallic Structures, *Key Eng. Mater.*, 2019, **813**, p 74–79. <https://doi.org/10.4028/www.scientific.net/KEM.813.74>
23. S. Adachi and N. Ueda, Wear and Corrosion Properties of Cold-Sprayed AISI 316L Coatings Treated by Combined Plasma Carburizing and Nitriding at Low Temperature, *Coatings*, 2018 <https://doi.org/10.3390/COATINGS8120456>
24. B. Dikici, H. Yilmazer, I. Ozdemir and M. Isik, The Effect of Post-Heat Treatment on Microstructure of 316L Cold-Sprayed Coatings and Their Corrosion Performance, *J. Therm. Spray*

- Technol.*, 2016, **25**(4), p 704–714. <https://doi.org/10.1007/s11666-016-0402-z>
25. S. Yin, J. Cizek, X. Yan and R. Lupoi, Annealing Strategies for Enhancing Mechanical Properties of Additively Manufactured 316L Stainless Steel Deposited by Cold Spray, *Surf. Coatings Technol.*, 2019, **370**, p 353–361. <https://doi.org/10.1016/j.surfcoat.2019.04.012>
  26. H. Assadi, H. Kreye, F. Gärtner and T. Klassen, Cold Spraying—A Materials Perspective, *Acta Mater.*, 2016, **116**, p 382–407. <https://doi.org/10.1016/j.actamat.2016.06.034>
  27. M.R. Rokni, S.R. Nutt, C.A. Widener, V.K. Champagne and R.H. Hrabe, Review of Relationship Between Particle Deformation, Coating Microstructure, and Properties in High-Pressure Cold Spray, *J. Therm. Spray Technol.*, 2017, **26**(6), p 1308–1355. <https://doi.org/10.1007/s11666-017-0575-0>
  28. M. Tului, C. Bartuli, A. Bezzon, A.L. Marino, F. Marra, S. Matera and G. Pulci, Amorphous Steel Coatings Deposited by Cold-Gas Spraying, *Metals (Basel)*, 2019 <https://doi.org/10.3390/met9060678>
  29. J. Cizek, M. Vilemova, F. Lukac, M. Koller, J. Kondas and R. Singh, Cold Sprayed Tungsten Armor for Tokamak First Wall, *Coatings*, 2019, **9**(12), p 1–15. <https://doi.org/10.3390/coatings9120836>
  30. S. Yin, W. Li, B. Song, X. Yan, M. Kuang, Y. Xu, K. Wen and R. Lupoi, Deposition of FeCoNiCrMn High Entropy Alloy (HEA) Coating via Cold Spraying, *J. Mater. Sci. Technol.*, 2019, **35**(6), p 1003–1007. <https://doi.org/10.1016/j.jmst.2018.12.015>
  31. Y. Xu, W. Li, L. Qu, X. Yang, B. Song, R. Lupoi and S. Yin, Solid-State Cold Spraying of FeCoCrNiMn High-Entropy Alloy: An Insight into Microstructure Evolution and Oxidation Behavior at 700–900 °C, *J. Mater. Sci. Technol.*, 2021, **68**, p 172–183. <https://doi.org/10.1016/j.jmst.2020.06.041>
  32. J. Lehtonen, H. Koivuluoto, Y. Ge, A. Juselius and S.P. Hannula, Cold Gas Spraying of a High-Entropy CrFeNiMn Equiatomic Alloy, *Coatings*, 2020 <https://doi.org/10.3390/coatings10010053>
  33. R.F. Vaz, A. Silvello, J. Sanchez, V. Albaladejo and I. García-Cano, The Influence of the Powder Characteristics on 316L Stainless Steel Coatings Sprayed by Cold Gas Spray, *Coatings*, 2021, **11**(2), p 1–18. <https://doi.org/10.3390/coatings11020168>
  34. A.S.M. Ang and C.C. Berndt, A Review of Testing Methods for Thermal Spray Coatings, *Int. Mater. Rev.*, 2014, **59**(4), p 179–223. <https://doi.org/10.1179/1743280414Y.0000000029>
  35. J. Lehtonen, Y. Ge, N. Ciftci, O. Heczko, V. Uhlenwinkel and S.P. Hannula, Phase Structures of Gas Atomized Equiatomic CrFeNiMn High Entropy Alloy Powder, *J. Alloys Compd.*, 2020, **827**, 154142. <https://doi.org/10.1016/j.jallcom.2020.154142>
  36. D. Wu, J.S.C. Jang and T.G. Nieh, Elastic and Plastic Deformations in a High Entropy Alloy Investigated Using a Nanoindentation Method, *Intermetallics*, 2016, **68**, p 118–127. <https://doi.org/10.1016/j.intermet.2015.10.002>
  37. M. Dada, P. Popoola, N. Mathe, S. Adeosun and S. Pityana, Investigating the Elastic Modulus and Hardness Properties of a High Entropy Alloy Coating Using Nanoindentation, *Int. J. Light. Mater. Manuf.*, 2021, **4**(3), p 339–345. <https://doi.org/10.1016/j.ijlmm.2021.04.002>
  38. S. Sinha, R.A. Mirshams, T. Wang, S.S. Nene, M. Frank, K. Liu and R.S. Mishra, Nanoindentation Behavior of High Entropy Alloys with Transformation-Induced Plasticity, *Sci. Rep.*, 2019, **9**(1), p 1–11. <https://doi.org/10.1038/s41598-019-43174-x>
  39. T. Goyal, R.S. Walia and T.S. Sidhu, Effect of Parameters on Coating Density for Cold Spray Process, *Mater. Manuf. Process.*, 2012, **27**(2), p 193–200. <https://doi.org/10.1080/10426914.2011.566906>
  40. D.L. Gilmore, R.C. Dykhuizen, R.A. Neiser, T.J. Roemer and M.F. Smith, Particle Velocity and Deposition Efficiency in the Cold Spray Process, *J. Therm. Spray Technol.*, 1999, **8**(4), p 576–582. <https://doi.org/10.1361/105996399770350278>
  41. R.S. Lima, A. Kucuk, C.C. Berndt, J. Karthikeyan, C.M. Kay and J. Lindemann, Deposition Efficiency, Mechanical Properties and Coating Roughness in Cold-Sprayed Titanium, *J. Mater. Sci. Lett.*, 2002, **21**(21), p 1687–1689. <https://doi.org/10.1023/A:1020833011448>
  42. S.V. Klinkov and V.F. Kosarev, Measurements of Cold Spray Deposition Efficiency, *J. Therm. Spray Technol.*, 2006, **15**(3), p 364–371. <https://doi.org/10.1361/105996306X124365>
  43. A. Silvello, P.D. Cavaliere, V. Albaladejo, A. Martos, S. Dosta and I.G. Cano, Powder Properties and Processing Conditions Affecting Cold Spray Deposition, *Coatings*, 2020, **10**(2), p 91. <https://doi.org/10.3390/coatings10020091>
  44. P. Cavaliere, A. Silvello, N. Cinca, H. Canales, S. Dosta, I. Garcia Cano and J.M. Guilemany, Microstructural and Fatigue Behavior of Cold Sprayed Ni-Based Superalloys Coatings, *Surf. Coat. Technol.*, 2017, **324**, p 390–402. <https://doi.org/10.1016/j.surfcoat.2017.06.006>
  45. R.F. Vaz, A. Silvello, J. Sanchez, V. Albaladejo and I. García-Cano, The Influence of the Powder Characteristics on 316L Stainless Steel Coatings Sprayed by Cold Gas Spray, *Coatings*, 2021 <https://doi.org/10.3390/coatings11020168>
  46. J. Pattison, S. Celotto, A. Khan and W. O'Neill, Standoff Distance and Bow Shock Phenomena in the Cold Spray Process, *Surf. Coatings Technol.*, 2008, **202**(8), p 1443–1454. <https://doi.org/10.1016/j.surfcoat.2007.06.065>
  47. L.-V. Bouthier, E. Hachem, *Analysis and Comparisons of Various Models in Cold Spray Simulations: Towards High Fidelity Simulations* (2020), pp. 1–29
  48. T. Kim, J. Lee, C. Park, H. Jo, M. Kim, *Fabrication of Transparent and Conducting Films of Self-Fused Silver Nanowires on Flexible Polyimide Substrates by Supersonic Spraying*, pp. 2–22
  49. T. Schmidt, H. Assadi, F. Gärtner, H. Richter, T. Stoltenhoff, H. Kreye and T. Klassen, From Particle Acceleration to Impact and Bonding in Cold Spraying, *J. Therm. Spray Technol.*, 2009, **18**(5–6), p 794–808. <https://doi.org/10.1007/s11666-009-9357-7>
  50. R.A. Seraj, A. Abdollah-zadeh, S. Dosta, H. Canales, H. Assadi and I.G. Cano, The Effect of Traverse Speed on Deposition Efficiency of Cold Sprayed Stellite 21, *Surf. Coatings Technol.*, 2019, **366**, p 24–34. <https://doi.org/10.1016/j.surfcoat.2019.03.012>
  51. W. Wong, P. Vo, E. Irissou, A.N. Ryabinin, J.G. Legoux and S. Yue, Effect of Particle Morphology and Size Distribution on Cold-Sprayed Pure Titanium Coatings, *J. Therm. Spray Technol.*, 2013, **22**(7), p 1140–1153. <https://doi.org/10.1007/s11666-013-9951-6>
  52. K. Spencer and M.X. Zhang, Optimisation of Stainless Steel Cold Spray Coatings Using Mixed Particle Size Distributions, *Surf. Coatings Technol.*, 2011, **205**(21–22), p 5135–5140. <https://doi.org/10.1016/j.surfcoat.2011.05.020>
  53. M. Torrell, S. Dosta, J.R. Miguel and J.M. Guilemany, Optimisation of HVOF Thermal Spray Coatings for Their Implementation as MSWI Superheater Protectors, *Corros. Eng. Sci. Technol.*, 2010, **45**(1), p 84–93. <https://doi.org/10.1179/147842209X12601838533508>
  54. J.M. Guilemany, M. Torrell and J.R. Miguel, Study of the HVOF Ni-Based Coatings' Corrosion Resistance Applied on Municipal Solid-Waste Incinerators, *J. Therm. Spray Technol.*, 2008, **17**(2), p 254–262. <https://doi.org/10.1007/s11666-008-9167-3>
  55. H. Assadi, T. Schmidt, H. Richter, J.O. Kliemann, K. Binder, F. Gärtner, T. Klassen and H. Kreye, On Parameter Selection in Cold Spraying, *J. Therm. Spray Technol.*, 2011, **20**(6), p 1161–1176. <https://doi.org/10.1007/s11666-011-9662-9>
  56. Y. Xiong, K. Kang, G. Bae, S. Yoon and C. Lee, Dynamic Amorphization and Recrystallization of Metals in Kinetic Spray

- Process, *Appl. Phys. Lett.*, 2008, **92**(19), p 19–21. <https://doi.org/10.1063/1.2928218>
57. F. Tang, L. Ajdelsztajn, G.E. Kim, V. Provenzano and J.M. Schoenung, Effects of Surface Oxidation during HVOF Processing on the Primary Stage Oxidation of a CoNiCrAlY Coating, *Surf. Coatings Technol.*, 2004, **185**(2–3), p 228–233. <https://doi.org/10.1016/j.surfcoat.2003.11.020>
58. B. Song, M. Bai, K.T. Voisey and T. Hussain, Role of Oxides and Porosity on High-Temperature Oxidation of Liquid-Fueled HVOF Thermal-Sprayed Ni50Cr Coatings, *J. Therm. Spray Technol.*, 2017, **26**(3), p 554–568. <https://doi.org/10.1007/s11666-017-0531-z>
59. P. Poza and M.Á. Garrido-Maneiro, Cold-Sprayed Coatings: Microstructure, Mechanical Properties, and Wear Behaviour, *Prog. Mater. Sci.*, 2021 <https://doi.org/10.1016/j.pmatsci.2021.100839>
60. S. Yin, J. Cizek, J. Cupera, M. Hassani, X. Luo, R. Jenkins, Y. Xie, W. Li and R. Lupoi, Formation Conditions of Vortex-like Intermixing Interfaces in Cold Spray, *Mater. Des.*, 2021, **200**, 109444. <https://doi.org/10.1016/j.matdes.2020.109444>
61. R. Huang, M. Sone, W. Ma and H. Fukunuma, The Effects of Heat Treatment on the Mechanical Properties of Cold-Sprayed Coatings, *Surf. Coatings Technol.*, 2015, **261**, p 278–288. <https://doi.org/10.1016/j.surfcoat.2014.11.017>
62. T. Hussain, D.G. McCartney, P.H. Shipway and D. Zhang, Bonding Mechanisms in Cold Spraying: The Contributions of Metallurgical and Mechanical Components, *J. Therm. Spray Technol.*, 2009, **18**(3), p 364–379. <https://doi.org/10.1007/s11666-009-9298-1>
63. S. Gu and S. Kamnis, Bonding Mechanism from the Impact of Thermally Sprayed Solid Particles, *Metall. Mater. Trans. A Phys. Metall. Mater. Sci.*, 2009, **40**(11), p 2664–2674. <https://doi.org/10.1007/s11661-009-9959-1>
64. H. Liao, B. Normand and C. Coddet, Influence of Coating Microstructure on the Abrasive Wear Resistance of WC/Co Cermet Coatings, *Surf. Coat. Technol.*, 2000, **124**(2–3), p 235–242. [https://doi.org/10.1016/S0257-8972\(99\)00653-2](https://doi.org/10.1016/S0257-8972(99)00653-2)
65. M.S. Mahdipoor, F. Tarasi, C. Moreau, A. Dolatabadi and M. Medraj, HVOF Sprayed Coatings of Nano-Agglomerated Tungsten-Carbide/Cobalt Powders for Water Droplet Erosion Application, *Wear*, 2015, **330–331**, p 338–347. <https://doi.org/10.1016/j.wear.2015.02.034>
66. M.E. Ibrahim, M. Medraj, *Water Droplet Erosion Ofwind Turbine Blades: Mechanics, Testing, Modeling and Future Perspectives*, vol. 13 (2020). <https://doi.org/10.3390/ma13010157>
67. P.H. Shipway and K. Gupta, The Potential of WC-Co Hardmetals and HVOF Sprayed Coatings to Combat Water-Droplet Erosion, *Wear*, 2011, **271**(9–10), p 1418–1425. <https://doi.org/10.1016/j.wear.2010.12.058>
68. R.F. Vaz, G.B. Sucharski, A. Chicoski, I.B.A.F. Siqueira, R. Tristante and A.G.M. Pukasiewicz, Comparison of FeMnCrSi Cavitation Resistance Coatings Deposited by Twin-Wire Electric Arc and High-Velocity Oxy-Fuel Processes, *J. Therm. Spray Technol.*, 2021, **30**(3), p 754–771. <https://doi.org/10.1007/s11666-020-01145-z>
69. M.S. Lamana, A.G.M. Pukasiewicz and S. Sampath, Influence of Cobalt Content and HVOF Deposition Process on the Cavitation Erosion Resistance of WC-Co Coatings, *Wear*, 2017, **2018**(398–399), p 209–219. <https://doi.org/10.1016/j.wear.2017.12.009>

**Publisher's Note** Springer Nature remains neutral with regard to jurisdictional claims in published maps and institutional affiliations.